TRAPPING OF PLANAR BROWNIAN MOTION: FULL FIRST PASSAGE TIME DISTRIBUTIONS BY KINETIC MONTE-CARLO, ASYMPTOTIC AND BOUNDARY INTEGRAL METHODS.

JAKE CHERRY, ALAN E. LINDSAY, ADRIÁN NAVARRO HERNÁNDEZ AND BRYAN QUAIFE

Abstract. We consider the problem of determining the arrival statistics of unbiased planar random walkers to complex target configurations. In contrast to problems posed in finite domains, simple moments of the distribution, such as the mean (MFPT) and variance, are not defined and it is necessary to obtain the full arrival statistics. We describe several methods to obtain these distributions and other associated quantities such as splitting probabilities. One approach combines a Laplace transform of the underlying parabolic equation with matched asymptotic analysis followed by numerical transform inversion. The second approach is similar, but uses a boundary integral equation method to solve for the Laplace transformed variable. To validate the results of this theory, and to obtain the arrival time statistics in very general configurations of absorbers, we introduce an efficient Kinetic Monte Carlo (KMC) method that describes trajectories as a combination of large but exactly solvable projection steps. The effectiveness of these methodologies is demonstrated on a variety of challenging examples highlighting the applicability of these methods to a variety of practical scenarios, such as source inference. A particularly useful finding arising from these results is that homogenization theories, in which complex configurations are replaced by equivalent simple ones, are remarkably effective at describing arrival time statistics.

1. Introduction. We consider the problem of describing the full arrival time distribution of diffusing particles to complex absorbing sets in planar regions $\mathbb{R}^2 \setminus \Omega$ (see Fig. 1). For a particle released from location $\mathbf{x}_0 \in \mathbb{R}^2 \setminus \Omega$, the central quantities of interest are its occupation density $p(\mathbf{x}, t; \mathbf{x}_0)$ and its survival probability $P(t; \mathbf{x}_0) = \int_{\mathbb{R}^2 \setminus \Omega} p(\mathbf{x}, t; \mathbf{x}_0) \, d\mathbf{x}$ together with the dependence on the number and location of absorbing sites. Our new contributions are several new efficient numerical and asymptotic methods to rapidly determine these quantities in the presence of complex configurations of targets (cf. Fig. 1).
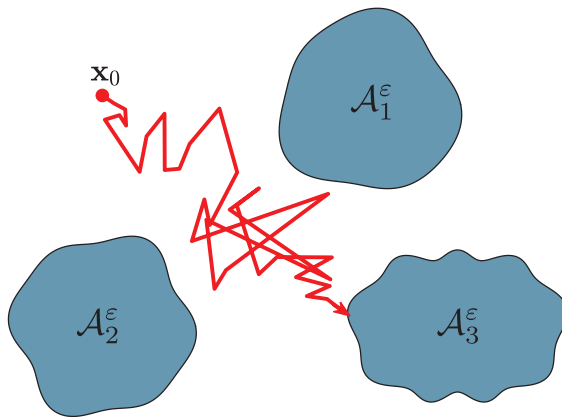

FIG. 1. *Schematic of planar Brownian motion to a collection of targets $\Omega := \cup_{j=1} \mathcal{A}_j^\varepsilon$. We consider the vanishing limit $\mathcal{A}_j^\varepsilon \to \mathbf{x}_j$ as $\varepsilon \to 0$ and specifically parameterize targets as $\mathcal{A}_j^\varepsilon = \mathbf{x}_j + \varepsilon \mathcal{A}_j$ to accommodate individual target geometries $\mathcal{A}_j$. Each target can be combinations of absorbing and reflecting sections.*

The general problem takes the form of a diffusion equation in $\mathbf{x} \in \mathbb{R}^2 \setminus \Omega$ where $\Omega := \cup_{j=1} \mathcal{A}_j^\varepsilon$ is a collection of targets, each with effective "radius" $\mathcal{O}(\varepsilon)$. In the vanishing limit $\varepsilon \to 0$, we solve for the probability

$p(\mathbf{x}, t; \mathbf{x}_0)$ of a particle originating at $\mathbf{x}_0$ being free at position $\mathbf{x}$ at time t. This probability density solves the exterior parabolic problem

$$\text{(1.1a)} \qquad \frac{\partial p}{\partial t} = D\Delta p, \qquad \mathbf{x} \in \mathbb{R}^2 \setminus \Omega, \quad t > 0; \qquad p(\mathbf{x}, 0) = \delta(\mathbf{x} - \mathbf{x}_0), \quad \mathbf{x} \in \mathbb{R}^2 \setminus \Omega;$$

$$\text{(1.1b)} \qquad p = 0, \quad \mathbf{x} \in \partial\Omega_a; \qquad D\nabla p \cdot \mathbf{n} = 0, \quad \mathbf{x} \in \partial\Omega_r,$$

where D is the diffusivity of the particle and Ω is a subset of $\mathbb{R}^2$. The boundary $\partial\Omega$ is partitioned into an absorbing set Ω_a and its impermeable complement Ω_r where reflecting boundary conditions are applied. We choose $\mathbf{n}$, the normal to the surface $\partial\Omega$, to point into the bulk. Some key quantities of interest for which rapid and accurate determination is desirable include the fluxes over each target, the splitting probabilities (likelihood particle encounters a certain target first) and the arrival time distribution. The survival probability

$$P(t; \mathbf{x}_0) = \int_{\mathbb{R}^2 \setminus \Omega} p(\mathbf{x}, t; \mathbf{x}_0) \, d\mathbf{x},$$

is another important quantity obtained, together with its dependence on the number and location of targets.

First passage time problems and their variants appear in a variety of disparate applications from cellular biology [6–8, 25], ecology [2, 24, 32, 44], and electrostatics [10]. A few comprehensive survey references can be found here [5, 17, 38, 39]. Preceding works on the theory of first arrival times to small absorbing sites have largely focussed on determining moments such as the mean first passage time (MFPT) [11, 17, 20–22, 35, 36] and in some cases the variance [24, 28, 30]. In the present scenario of an unbounded domain, these moments are not finite [38, 39] and we must therefore seek the full distribution of arrival times. In the scenario where diffusion occurs in a bounded domain, the full arrival time distributions to small absorbing targets have been considered in two [7, 30] and three [6, 19] dimensions.

In the planar (unbounded) scenario considered here, capture is guaranteed; however, it may occur over very long timescales. This becomes apparent from the arrival time distribution $\chi_0(t)$ for a particle of diffusivity $D = 1$, initially at distance R from a target disc of unit radius centered at the origin. This distribution $\chi_0(t)$ and its large time behavior (see [39] and Appendix A) are given by

$$\text{(1.2)} \qquad \chi_0(t) = \frac{2}{\pi} \int_0^\infty \left[\frac{J_0(\omega)Y_0(\omega R) - J_0(\omega R)Y_0(\omega)}{Y_0^2(\omega) + J_0^2(\omega)} \right] \omega e^{-\omega^2 t} \, d\omega = \mathcal{O}\left(\frac{1}{t \log^2 t} \right), \qquad t \to \infty,$$

where $J_0(z)$, $Y_0(z)$ are Bessel functions. The slow rate of decay in the tail of this distribution reveals that very long arrival times are typical (see Fig. 5(a)). For example, when $R = 10$, a particle with diffusivity $D = 1$ still has an approximately 20% chance of being free after $t = 10^{10}$. Equilibrium quantities (e.g. splitting probabilities) therefore emerge on timescales that may not necessarily be the most biologically meaningful. For example, in applications such as a moth's search for a mate [44], or cellular signaling where a downstream event initializes as soon as a molecule reaches a receptor [25], the statistics of particles which reach the target first are of most interest. These *extreme statistics* are governed by the behavior of $P(t; \mathbf{x}_0)$ for $t \ll 1$ [26] and so it is necessary to have methodologies for determining full distributions of arrival time statistics.

In the present work, we outline several methods to solve (1.1). First, in Sec. 2 we apply a Laplace transform

$\hat{p}(\mathbf{x}, s) = \int_{t=0}^{\infty} p(\mathbf{x}, t)e^{-st} dt$ to (1.1) to arrive at an elliptic problem of modified Helmholtz type

$$\text{(1.3a)} \qquad D\Delta\hat{p} - s\,\hat{p} = -\delta(\mathbf{x} - \mathbf{x}_0), \qquad \mathbf{x} \in \mathbb{R}^2 \setminus \Omega;$$

$$\text{(1.3b)} \qquad \hat{p} = 0 \quad \mathbf{x} \in \Omega_a; \qquad \nabla\hat{p} \cdot \mathbf{n} = 0 \quad \mathbf{x} \in \Omega_r.$$

In the limit of well-separated traps, we solve the resulting transform problem in terms of an asymptotic expansion where solutions are obtained in terms of modified Helmholtz Green's function. This methodology was originally developed in [30] and recently applied in [6, 7] to the study of first passage times of particles with resetting. The Laplace transform is inverted numerically by Talbot quadrature [1] resulting in a hybrid numerical-asymptotic method. In Sec. 3, we take a similar approach, but replace the asymptotic solution of (1.3) with a layer potential representation. This results in a boundary integral equation that is solved numerically using a collocation method.

In Sec. 4 we develop a particle based kinetic Monte-Carlo (KMC) method that evaluates solutions of (1.1) by dividing the sojourn of particles into projection steps where exact solutions are available [18, 27]. This offers a rapid, accurate and easy to implement method for the solution of (1.1) in very general geometries. In Sec. 5 we demonstrate the applicability of these methods on a variety of examples. In particular, we provide numerical validation of previously derived homogenization theories and find them to be highly effective in reproducing the arrival time distributions. We also investigate the time dependent accumulation of signal into the targets which are observed to converge very slowly to the static splitting probabilities that describe the relative flux into each target. This suggests that a relevant physical or biological time scale should be considered before using receptor arrival information to make inferences on environmental conditions.

2. Asymptotic description of arrival times of particles diffusing in $\mathbb{R}^2$. In this section we use matched asymptotic expansions to derive an approximation for the density of a particle diffusing in $\mathbb{R}^2 \setminus \Omega$ in the presence of well-separated target sites. We assume N targets $\mathcal{A}_j^{\varepsilon}$ with centers $\{\mathbf{x}_j\}_{j=1}^N$ so that $\mathcal{A}_j^{\varepsilon} = \mathbf{x}_j + \varepsilon\mathcal{A}_j$ and $\mathcal{A}_j$ is a rescaling of the target. The collection of target sites are then described by

$$\text{(2.4)} \qquad \Omega = \bigcup_{j=1}^{N}(\mathbf{x}_j + \varepsilon\mathcal{A}_j),$$

where ε is a parameter controlling the extent of the targets and enforces the well-separated condition as $\varepsilon \to 0$. The geometry of individual targets $\mathcal{A}_j$ can be quite general.

The aim is to solve the solution of the initial-boundary value problem (1.1) and determine the free probability $P(t) = \int_{\Omega} p(\mathbf{x}, t) d\mathbf{x}$ together with the capture time density $C(t) = -P'(t)$. The first step [30] in the analysis is to define, for $s \in \mathbb{C}$, the Laplace transform $\hat{p}(\mathbf{x}, s) = \int_{t=0}^{\infty} p(\mathbf{x}, t)e^{-st} dt$ that solves (1.3). The mixed boundary conditions (1.3b) indicate that the target boundary may have a combination of absorbing or reflecting components so that $\partial\Omega = \Omega_a \cup \Omega_r$. In the absence of the target set Ω, the solution $\hat{p}$ of (1.3) is defined in terms of the free space modified Helmholtz Green's function $G_h(\mathbf{x}; \boldsymbol{\xi}, s)$

$$\text{(2.5a)} \qquad D\Delta G_h - s\,G_h = -\delta(\mathbf{x} - \boldsymbol{\xi}), \qquad \mathbf{x} \in \mathbb{R}^2 \setminus \{\boldsymbol{\xi}\};$$

$$\text{(2.5b)} \qquad G_h(\mathbf{x}; \boldsymbol{\xi}, s) = \frac{1}{2\pi D}K_0(\sqrt{s/D}|\mathbf{x} - \boldsymbol{\xi}|), \qquad \int_{\mathbb{R}^2} G_h(\mathbf{x}; \boldsymbol{\xi}, s) d\mathbf{x} = \frac{1}{s};$$

$$\text{(2.5c)} \qquad G_h(\mathbf{x}; \boldsymbol{\xi}, s) \sim -\frac{1}{2\pi D}\log|\mathbf{x} - \boldsymbol{\xi}| + R_h(s) + \mathcal{O}(1), \qquad \mathbf{x} \to \boldsymbol{\xi}.$$

Here $R_h(s)$ is the regular part of $G_h(\mathbf{x}; \boldsymbol{\xi}, s)$ at the source. The small argument asymptotics $K_0(z) \sim -\log(z) + \log 2 - \gamma_e$ as $z \to 0$ give this self-interaction term to be

$$R_h(s) = \frac{1}{2\pi D}\left(\log 2 - \gamma_e - \log\sqrt{s/D}\right), \tag{2.6}$$

where $\gamma_e \approx 0.5772$ is the Euler-Mascheroni constant.

In the limit of well-separated absorbers $\varepsilon \to 0$, we employ a matched asymptotic analysis to replace each target (1.3b) by effective singularity conditions. To establish this singularity condition, the following change of variables is introduced near the jth absorber

$$\mathbf{y} = \frac{\mathbf{x} - \mathbf{x}_j}{\varepsilon}, \qquad v(\mathbf{y}) = \hat{p}(\mathbf{x}_j + \varepsilon\mathbf{y}). \tag{2.7}$$

In these coordinates, the transformed equation (1.3a) is $D\Delta_{\mathbf{y}}v - s\varepsilon^2 v = -\varepsilon^2\delta(\mathbf{x} - \mathbf{x}_0)$. In addition to the limit $\varepsilon \to 0$, we additionally consider the case $s\varepsilon^2 \ll 1$ which is valid provided s is not too large. The limit $s \to \infty$ corresponds to $t \to 0$ and therefore we cannot expect good agreement for arbitrarily short times. With these points in mind, we continue by considering the local solution $v(\mathbf{y}) = v_j(\mathbf{y}) + \mathcal{O}(\varepsilon)$ near the target where $v_j(\mathbf{y})$ satisfies the exterior problem

$$\Delta_{\mathbf{y}}v_j = 0, \quad \mathbf{y} \in \mathbb{R}^2/\mathcal{A}_j, \qquad v_j = 0, \quad \mathbf{y} \in \partial\mathcal{A}_j; \tag{2.8a}$$

$$v_j(\mathbf{y}) \sim \log|\mathbf{y}| - \log d_j + \mathcal{O}\left(\frac{1}{|\mathbf{y}|^2}\right), \qquad |\mathbf{y}| \to \infty. \tag{2.8b}$$

Here the parameter d_j is the logarithmic capacitance which depends on the shape of $\mathcal{A}_j$ and the boundary conditions applied to it. In section 2.2 we give an overview of many scenarios in which d_j can be calculated. The behavior of $v_j(\mathbf{y})$ at infinity gives the matching condition for $\hat{p}(\mathbf{x})$ as $\mathbf{x}$ approaches $\mathbf{x}_j$. That is,

$$\hat{p}(\mathbf{x}, s) \sim S_j\nu_j\left(\log\left|\frac{\mathbf{x} - \mathbf{x}_j}{\varepsilon}\right| - \log d_j\right) = S_j\nu_j\log|\mathbf{x} - \mathbf{x}_j| + S_j, \quad \mathbf{x} \to \mathbf{x}_j; \qquad \nu_j = -\frac{1}{\log\varepsilon d_j}, \tag{2.9}$$

where S_j is a strength term to be determined in terms of $(N + 1)$ parameters $(s, \boldsymbol{\nu}) = (s, \nu_1, \dots, \nu_N)$. Therefore, in the outer region away from targets, we pose the asymptotic expansion

$$\hat{p}(\mathbf{x}; s) = \hat{p}_0(\mathbf{x}; s, \boldsymbol{\nu}) + \varepsilon\,\hat{p}_1(\mathbf{x}; s, \boldsymbol{\nu}) + \mathcal{O}(\varepsilon), \qquad \varepsilon \to 0.$$

The leading order solution $\hat{p}_0(\mathbf{x}; s, \boldsymbol{\nu})$ "sums-the-logs" and is accurate to all logarithmic orders. The correction term $\hat{p}_1$, which we do not explicitly determine, describes how target orientation influences capture and can be found following methods outlined in [29]. The leading order problem satisfies

$$D\Delta\hat{p}_0 - s\,\hat{p}_0 = -\delta(\mathbf{x} - \mathbf{x}_0), \quad \mathbf{x} \in \mathbb{R}^2/\{\mathbf{x}_1, \dots, \mathbf{x}_N\}, \tag{2.10a}$$

$$\hat{p}_0 \sim S_j\nu_j\log|\mathbf{x} - \mathbf{x}_j| + S_j, \quad \mathbf{x} \to \mathbf{x}_j, \qquad j = 1, \dots, N. \tag{2.10b}$$

The solution $\hat{p}_0(\mathbf{x}, s)$ of (2.10) is described in terms of the modified Helmholtz Green's function (2.5) as

$$\hat{p}_0(\mathbf{x}, s) = G_h(\mathbf{x}; \mathbf{x}_0, s) - 2\pi D\sum_{j=1}^{N} S_j\nu_j G_h(\mathbf{x}; \mathbf{x}_j, s). \tag{2.11}$$

The coefficients S_j can be determined by equating the regular parts in (2.10b) and in (2.11). That is,

$$S_j = G_h(\mathbf{x}_j; \mathbf{x}_0, s) - 2\pi D\left[S_j\nu_j R_h(s) + \sum_{\substack{i=1 \\ i \neq j}}^{N} S_i\nu_i G_h(\mathbf{x}_j; \mathbf{x}_i, s)\right], \qquad j = 1, \dots, N. \tag{2.12}$$

In summary, we have that the transform equation (1.3) has asymptotic solution $p(\mathbf{x}; s) \sim p_0(\mathbf{x}; s) + \cdots$ as $\varepsilon \to 0$ where $p_0(\mathbf{x}; s)$ satisfies

(2.13a)
$$\hat{p}_0(\mathbf{x}, s) = G_h(\mathbf{x}; \mathbf{x}_0, s) - 2\pi D \sum_{j=1}^{N} S_j \nu_j G_h(\mathbf{x}; \mathbf{x}_j, s).$$

The strengths $\{S_j\}_{j=1}^{N}$ satisfy (2.12) which can be represented in compact matrix form as

(2.13b) $\quad (\mathcal{I} + 2\pi D \,\mathcal{G}_h \mathcal{V})\, \mathbf{S} = \mathbf{g}_0, \qquad [\mathcal{G}_h]_{i,j} = \begin{cases} R_h(s), & i = j, \\ G_h(\mathbf{x}_i; \mathbf{x}_j, s), & i \neq j. \end{cases} \qquad [\mathcal{V}]_{i,j} = \begin{cases} \nu_i & i = j, \\ 0, & i \neq j, \end{cases}$

where $\mathcal{I} \in \mathbb{R}^{N \times N}$ is the identity, $\mathbf{S} \in \mathbb{R}^N$ and $\mathbf{g}_0 \in \mathbb{R}^N$ are given by

(2.13c) $\qquad \mathbf{S} = [S_1, S_2, \ldots, S_N]^T, \qquad \mathbf{g}_0 = [G_h(\mathbf{x}_1; \mathbf{x}_0, s), G_h(\mathbf{x}_2; \mathbf{x}_0, s), \ldots, G_h(\mathbf{x}_N; \mathbf{x}_0, s)]^T.$

The matrix $\mathcal{G}$ describes the interactions between targets and their competition for flux while the vector $\mathbf{g}_0$ reflects the influence of the initial location on each of the targets. The vector $\widehat{\mathcal{J}} = 2\pi D \mathcal{V} \mathbf{S}(s)$ describes the transformed fluxes through each of the targets and is obtained from solving the linear system (2.13).

At this stage we calculate additional quantities of interest, namely the survival probability $P(t)$ and arrival time distribution $C(t)$. Using equation (2.11) and (2.5c), the Laplace transform $\hat{P}(s)$ of the free probability is given by

(2.14a)
$$\hat{P}(s) = \int_{\Omega} \hat{p}_0(\mathbf{x}, s)\, d\mathbf{x} = \int_{\Omega} G_h(\mathbf{x}; \mathbf{x}_0, s) d\mathbf{x} - 2\pi D \sum_{j=1}^{N} S_j \nu_j \int_{\Omega} G_h(\mathbf{x}; \mathbf{x}_j, s) d\mathbf{x} = \frac{1}{s}\left[1 - 2\pi D \sum_{j=1}^{N} \nu_j S_j(s)\right].$$

The relationship $C(t) = -P'(t)$, yields that the Laplace transform of the arrival time distribution $C(t)$ is

(2.14b)
$$\hat{C}(s) = -[s\hat{P}(s) - P(0)] = -s\hat{P}(s) + 1 = 2\pi D \sum_{j=1}^{N} \nu_j S_j(s).$$

2.1. Inverse Laplace Transform. To obtain $P(t)$ and $C(t)$ defined by (2.14), the inverse Laplace transform

(2.15)
$$P(t) = \frac{1}{2\pi i} \int_{\Gamma_B} e^{st} \hat{P}(s)\, ds,$$

must be evaluated where Γ_B is the Bromwich contour $\Gamma_B = \{\gamma + iy \,|\, -\infty < y < \infty\}$. The parameter γ is chosen so that all singularities of $\hat{P}(s)$ lie to the left of $\text{Re}(s) = \gamma$. In the present scenario associated with diffusive motion, the singularities of $\hat{P}(s)$ lie along the negative real axis due to the branch cut of $\sqrt{s}$. Rapid and effective numerical evaluation of (2.15) can be achieved by deforming the contour around $\text{Re}(s) = 0$ since the integrand of (2.15) decays very rapidly for $\text{Re}(s) < 0$. The Talbot contour Γ_T is a family of deformations (see Fig. 2) to Γ_B where

(2.16)
$$\Gamma_T = \{\sigma + \mu(\theta \cot \theta + \nu i\, \theta) \,|\, -\pi < \theta < \pi\},$$

and σ, μ and ν are parameters that control the curve shape [48, 49]. Rapid and accurate evaluation of the inverse Laplace transform is then achieved by applying the midpoint rule on this curve.
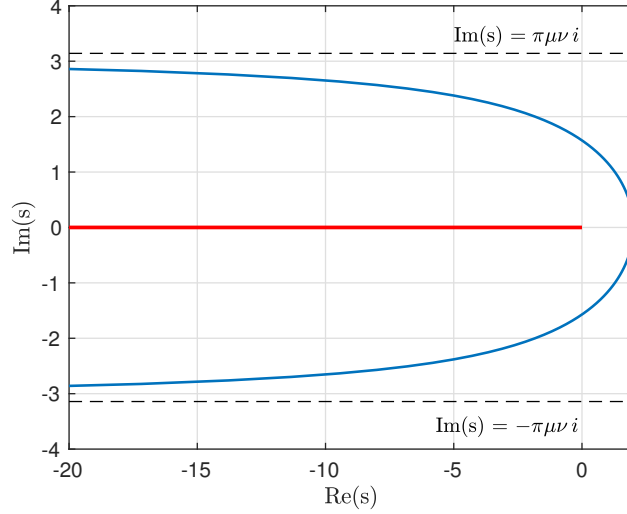
FIG. 2. *A schematic of the Talbot curve (2.16) for parameter values* $\sigma = 0$, $\mu = 2$, $\nu = 0.5$. *The red line indicates the singularities along the negative real line arising from the* $\sqrt{s}$ *singularity.*

2.2. Logarithmic capacitance for various shapes. The asymptotic solution (2.14) encodes the geometry of each target $\mathcal{A}_j$ into the logarithmic capacitance d_j, determined by the solution of (2.8). Here we discuss the determination of d_j and briefly recap known results for regular geometries and simple boundary conditions.

Regular geometric shapes. For simple shapes such as circles, ellipses, triangles and squares with all absorbing perimeters, the logarithmic capacitance is known exactly. A list of these quantities, reproduced from [24], is included in Table 1.

Shape of $\mathcal{A}_j$	Logarithmic capacitance d_j
circle of radius a	$d_j = a$
ellipse, semi-axes a, b	$d_j = \frac{a+b}{2}$
equilateral triangle, side-length h	$d_j = \frac{\sqrt{3}\Gamma(\frac{1}{3})^3 h}{8\pi^2} \approx 0.422h$
isosceles right triangle, side-length h	$d_j = \frac{3^{3/4}\Gamma(1/4)^2 h}{2^{7/2}\pi^{3/2}} \approx 0.476h$
square, side-length h	$d_j = \frac{\Gamma(1/2)^2 h}{4\pi^{3/2}} \approx 0.590h$

TABLE 1
The logarithmic capacitance of some simple geometries with absorbing boundary conditions, reproduced from [24].

Partially absorbing disk: Single window. For a circular trap that is absorbing except for the reflecting portion $\theta \in (-\sigma, \sigma)$, the problem (2.8) may be expressed in polar coordinates (r, θ) as

$$(2.17a) \qquad \Delta v = 0, \quad r \geq 1, \quad \theta \in (-\pi, \pi);$$

$$(2.17b) \qquad \partial_r v = 0, \quad r = 1, \quad \theta \in (-\sigma, \sigma); \qquad v = 0, \quad r = 1, \quad \theta \in (\sigma, \pi) \cup (-\pi, -\sigma);$$

$$(2.17c) \qquad v \sim \log r - \log d_c + \mathcal{O}(r^{-1}), \quad r \to \infty.$$

The separable solution of (2.17) takes the form of the cosine series

$$v(r, \theta) = \log r + \frac{a_0}{2} + \sum_{n=1}^{\infty} \frac{a_n}{r^n} \cos n\theta,$$

where the coefficients $\{a_n\}_{n=0}^{\infty}$ satisfy the dual trigonometric series

(2.18a)
$$\frac{a_0}{2} + \sum_{n=1}^{\infty} a_n \cos n\theta = 0, \quad \theta \in (\sigma, \pi),$$

(2.18b)
$$\sum_{n=1}^{\infty} n a_n \cos n\theta = 1, \quad \theta \in (0, \sigma).$$

The solution of (2.18) was determined in [29] from an integral equation theory which reveals that

(2.19)
$$-\log d_c = \frac{a_0}{2} = \frac{\sqrt{2}}{\pi} \int_0^\sigma \frac{u \sin \frac{u}{2}}{\sqrt{\cos u - \cos \sigma}} \, du.$$

For the half absorbing case ($\sigma = \pi/2$), $a_0 = 2 \log 2$, while in the singular mostly reflecting limit $\sigma \ll 1$, it can be determined that $a_0 \sim -4 \log \frac{\sigma}{2}$. In other scenarios, the integral (2.19) is readily evaluated by quadrature.

Partially absorbing disk: Multiple windows. In the scenario of a circular trap with N small absorbing windows of length σ centered at points $\{\mathbf{y}_j\}_{j=1}^N$, it was shown in [29] that as $\sigma \to 0$

(2.20a)
$$-\log d_c = \frac{a_0}{2} \sim -\frac{2}{N} \log \frac{\sigma}{4} - \frac{2}{N^2} \sum_{i=1}^N \log \prod_{\substack{j=1 \\ j \neq i}}^N |\mathbf{y}_i - \mathbf{y}_j|.$$

For windows centered at roots of unity $\mathbf{y}_j = \left(\cos \frac{2\pi j}{N}, \sin \frac{2\pi j}{N} \right)$, and for $N\sigma < 1$, (2.20a) reduces to

(2.20b)
$$-\log d_c = \frac{a_0}{2} = -\frac{2}{N} \log \frac{\sigma}{4} - \frac{2}{N^2} (N \log N) = -\frac{2}{N} \log \frac{\sigma N}{4}.$$

Partially absorbing disk: Homogenization limit. The results (2.20) can be used to identify an homogenization limit as $N \to \infty$ and $\sigma \to 0$. The absorbing fraction f is defined through $N\sigma = 2\pi f$ and the homogenized logarithmic capacitance problem satisfies

(2.21a)
$$\Delta v_h = 0, \quad r > 1; \qquad \sigma \frac{\partial v_h}{\partial r} + \kappa(f) v_h = 0, \quad r = 1;$$

(2.21b)
$$v_h \sim \log r - \log d_c + \cdots, \quad r \to \infty.$$

In the dilute limit $f \ll 1$, the homogenized parameters were identified in [29] to be

(2.21c)
$$\kappa(f) = -\frac{\pi f}{\log \frac{\pi f}{2}}, \qquad \log d_c = \frac{\sigma}{\kappa(f)}.$$

In Section 5.2, we show numerical results that validate this homogenized formulation and demonstrate that it is highly accurate in predicting the arrival time statistics of the full problem.

The logarithmic capacitance for a two trap cluster. In the case of two circular traps separated by distance ℓ, it was derived in [24] (see also [20, 35, 40, 45]) from an expansion in bi-polar coordinates that

(2.22)
$$\log d_c = \frac{1}{2} \log(\ell^2 - 4) - \frac{\beta}{2} + \sum_{k=1}^{\infty} \frac{e^{-k\beta}}{k \cosh(k\beta)}, \qquad \beta = \cosh^{-1}\left(\frac{\ell}{2}\right).$$

Numerical evaluation of the logarithmic capacitance for general configurations. For very general configurations of clusters, the logarithmic capacitance problem (2.8) can be obtained numerically by a boundary integral approach [14]. Another approach developed in [20, 35], and based on works [10, 47], is to develop a series solution of (2.8) followed by a least squared method to obtain the unknown coefficients. For the case of m circular absorbers with centers $\{c_j\}_{j=1}^m$, the series takes the form

$$(2.23) \qquad v(z) = -\log d_c + \sum_{j=1}^m e_j \log |z - c_j| + \sum_{j=1}^m \sum_{k=1}^n \left(a_{jk} \text{Re}(z - c_j)^{-k} + b_{jk} \text{Im}(z - c_j)^{-k} \right), \quad z \in \mathbb{C}.$$

The constants d_c, e_j, a_{jk}, b_{jk} are to be determined while $\sum_{j=1}^m e_j = 1$ enforces the far field behavior $v \sim \log |z|$ as $|z| \to \infty$. A system for the unknown constants is formed by evaluating (2.23) at a collection of boundary points along which $v = 0$. A similar methodology was used in [29] to solve a truncated version of the dual trigonometric series (2.18) by evaluation at a set of boundary values followed by least squared solution.

3. Boundary integral equation description of arrival times of particles diffusing in $\mathbb{R}^2$. An alternative approach to matched asymptotics for solving (1.1) is to use an integral equation approach. Integral equations are a natural choice for unbounded complex domains such as the one in Fig. 1 since they easily resolve complex geometries while automatically satisfying the far-field boundary conditions. Others have applied integral equation methods to solve (1.1) using the full space-time heat kernel [16] or by discretizing in time and solving the resulting elliptic PDE with an integral equation formulation [9, 23]. However, these approaches have several challenges that include maintaining long time histories and computing volume integrals. We take a new approach by solving for the Laplace transformed variable $\hat{p}(\mathbf{x}, s)$ that satisfies (1.3). We only consider the case where $\partial\Omega$ is absorbing so that the boundary condition is Dirichlet and homogeneous.

We begin by writing $\hat{p}$ as the sum of a particular and homogeneous solution of (1.3)

$$\hat{p}(\mathbf{x}, s) = G_h(\mathbf{x}; \mathbf{x}_0, s) + \hat{p}^H(\mathbf{x}, s),$$

where G_h is the free space modified Helmholtz Green's function (2.5). Using the boundary condition (1.3b), $\hat{p}^H$ satisfies the homogeneous PDE

$$(3.24a) \qquad\qquad\qquad\qquad D\Delta\hat{p}^H - s\hat{p}^H = 0, \qquad \mathbf{x} \in \Omega,$$

$$(3.24b) \qquad\qquad\qquad\qquad \hat{p}^H(\mathbf{x}) = f(\mathbf{x}), \quad \mathbf{x} \in \partial\Omega,$$

where $f(\mathbf{x}) = -G_h(\mathbf{x}; \mathbf{x}_0, s)$. We represent the solution of (3.24) with the double-layer potential

$$\hat{p}^H(\mathbf{x}) = \mathcal{D}[\sigma](\mathbf{x}) = \int_{\partial\Omega} \frac{\partial}{\partial \mathbf{n_y}} G_h(\mathbf{x}; \mathbf{y}, s)\sigma(\mathbf{y})\, ds_{\mathbf{y}}, \quad \mathbf{x} \in \Omega,$$

where σ is an unknown density function. We remind the reader that the unit normal $\mathbf{n_y}$ points into the bulk. To satisfy the boundary condition (3.24b), the density function must solve

$$(3.25) \qquad\qquad\qquad f(\mathbf{x}) = \frac{1}{2}\sigma(\mathbf{x}) + \mathcal{D}[\sigma](\mathbf{x}), \quad \mathbf{x} \in \partial\Omega.$$

A numerical solution of the second-kind integral equation (3.25) is formed by discretizing $\partial\Omega$ at N quadrature points and approximating the integrals with the trapezoid rule. The resulting linear system is

$$(3.26) \qquad\qquad f(\mathbf{x}_i) = \frac{1}{2}\sigma(\mathbf{x}_i) + \frac{1}{2\pi}\sum_{j=1}^N G_h(\mathbf{x}_i; \mathbf{x}_j, s)\sigma(\mathbf{x}_j)\,\Delta s_j, \quad i = 1, \ldots, N,$$

and the diagonal term of this linear system is replaced with the limiting value

$$\lim_{\substack{\mathbf{y} \to \mathbf{x} \\ \mathbf{x} \in \partial\Omega}} G_h(\mathbf{x}; \mathbf{y}, s) = -\frac{1}{2}\kappa(\mathbf{x}),$$

where $\kappa(\mathbf{x})$ is the curvature of $\partial\Omega$. The linear system (3.26) is solved with the generalized minimal residual method (GMRES), and since it is the discretization of a second-kind integral equation, the number of required iterations is mesh-independent. This method to solve for $\hat{p}(\mathbf{x}, s)$ is coupled with the inverse Laplace transform (2.15), where we use the same Talbot contour illustrated in Fig. 2.

The flux at point $\mathbf{x} \in \partial\Omega$ and time t is $\mathcal{J}(\mathbf{x}, t) = \frac{\partial}{\partial\mathbf{n}}p(\mathbf{x}, t)$. Since we write $\hat{p}(\mathbf{x}, s)$ as the sum of a fundamental solution and a homogeneous solution, we compute the flux of these terms individually, and the flux due to the fundamental solution is computed analytically. The flux due to the homogeneous solution $\hat{p}^H$ is

(3.27) $$\widehat{\mathcal{J}}^H(\mathbf{x}; s) = \frac{\partial}{\partial\mathbf{n_x}}\mathcal{D}[\sigma](\mathbf{x}) = \int_{\partial\Omega} \frac{\partial}{\partial\mathbf{n_x}} \frac{\partial}{\partial\mathbf{n_y}} G_h(\mathbf{x}; \mathbf{y}, s)\sigma(\mathbf{y})\, ds_{\mathbf{y}},$$

which needs to be estimated with quadrature. As $\mathbf{x} \to \mathbf{y}$, the integrand of (3.27) satisfies

$$\frac{\partial}{\partial\mathbf{n_x}} \frac{\partial}{\partial\mathbf{n_y}} G_h(\mathbf{x}; \mathbf{y}, s) \sim \|\mathbf{x} - \mathbf{y}\|^{-2},$$

and the trapezoid rule cannot be used. An alternative quadrature rule uses the odd-indexed quadrature points for even-indexed discretization points, and uses the even-indexed quadrature points for odd-indexed discretization points [43]. However, this odd-even integration quadrature rule converges only when the singularity of the integrand is no stronger than $\|\mathbf{x} - \mathbf{y}\|^{-1}$.

To formulate the normal derivative of the double-layer potential with a tractable integrand, we first add and subtract the leading order asymptotics of G_h described in (2.5c). That is, $\widehat{\mathcal{J}}^H(\mathbf{x}; s) = I_1 - I_2$ where

$$I_1 = \int_{\partial\Omega} \frac{\partial}{\partial\mathbf{n_x}} \frac{\partial}{\partial\mathbf{n_y}} \left(G_h(\mathbf{x}; \mathbf{y}, s) + \frac{1}{2\pi} \log|\mathbf{x} - \mathbf{y}| \right) \sigma(\mathbf{y})\, ds_{\mathbf{y}},$$

$$I_2 = \int_{\partial\Omega} \frac{\partial}{\partial\mathbf{n_x}} \frac{\partial}{\partial\mathbf{n_y}} \left(\frac{1}{2\pi} \log|\mathbf{x} - \mathbf{y}| \right) \sigma(\mathbf{y})\, ds_{\mathbf{y}}.$$

The singularity of the integrand in I_1 behaves as $\|\mathbf{x} - \mathbf{y}\|^{-1}$, and odd-even integration can be applied. The integral I_2 is further decomposed as

$$I_2 = \frac{1}{2\pi} \int_{\partial\Omega} \frac{\partial}{\partial\mathbf{n_x}} \frac{\partial}{\partial\mathbf{n_y}} \log|\mathbf{x} - \mathbf{y}|(\sigma(\mathbf{y}) - \sigma(\mathbf{x}))\, ds_{\mathbf{y}} - \frac{\sigma(\mathbf{x})}{2\pi} \int_{\partial\Omega} \frac{\partial}{\partial\mathbf{n_x}} \frac{\partial}{\partial\mathbf{n_y}} \log|\mathbf{x} - \mathbf{y}|\, ds_{\mathbf{y}}.$$

The second integral in this expression is the normal derivative of a constant function, and therefore is zero. The remaining integral has an integrand with a singularity that also behaves as $\|\mathbf{x} - \mathbf{y}\|^{-1}$, and odd-even integration can be applied.

Having developed a quadrature method to compute $\widehat{\mathcal{J}}^H(\mathbf{x}; s)$, the point-wise flux can be computed at time t by applying the midpoint rule along the Talbot contour in Fig. 2. Then, the total flux into $\partial\Omega$ can easily be computed by applying the trapezoid rule to

$$S(t) = \int_{\partial\Omega} \mathcal{J}(s, t)\, ds.$$

4. Particle based Kinetic Monte Carlo simulations. Monte Carlo simulations provide a valuable tool for numerically estimating the distribution of capture times of diffusing particles for problems such as (1.1) and have been used extensively [4, 31, 33, 34]. Trajectories associated to the density (1.1) can be constructed through the discretization

$$(4.28) \qquad \mathbf{x}(t + dt) = \mathbf{x}(t) + \sqrt{2Ddt}\, Z, \qquad \mathbf{x}(0) = \mathbf{x}_0,$$

where $Z \sim N(0, 1)$. The sequence of small displacements (4.28) terminates when the particle encounters the absorbing surface $\partial\Omega_a$. The algorithm is repeated for many particles (millions or even billions) to sample the capture time distribution. This approach is flexible and easy to implement but hampered by a set of problems.

If a fixed stepsize dt is adopted, errors are introduced at that lengthscale that accrue near boundaries. First, for a capture event in the interval $(t, t + dt)$, we typically choose $t + dt$ as the arrival time which is an overestimate. Second, trajectories drawn from (4.28) will necessarily miss some encounters with boundaries and therefore overestimate the hitting time. Another challenge is that capture problems associated with (1.1) are notorious for their fat-tailed distributions, i.e., a significant fraction of realizations undergo long excursions before capture. A key component of any efficient method is adaptivity in stepsize since a trajectory of (4.28) simulated with a fixed step method will take a very long time to reach an absorbing site.

4.1. Kinetic Monte Carlo (KMC) method for simulation of planar diffusion to absorbers. Decreasing the step size in an adaptive manner based on distance to target can ameliorate these issues. The Kinetic Monte Carlo (KMC) method [3] maximizes this opportunity by advancing the diffusion process in a spatial stepsize corresponding to the distance to the target, $d(\mathbf{x}_0, \partial\Omega)$. The geometry of each step can take many forms, but it should be chosen such that the details of the sojourn can be rapidly and accurately sampled from closed form expressions. Similar ideas have been employed in N-body simulations of kinetic gases [34], chemical reactions [50] and epitaxial crystal growth [41, 42, 46]. In this paper we describe implementation details and rudimentary analysis of such a scheme that can handle complex geometries and mixed boundary conditions. This method completely bypasses the need to advance particles based on discretized steps such as (4.28).

Setup. We adopt a piecewise linear representation for the boundary $\partial\Omega$ of the target set Ω based on vertexes with M straight edges $\partial\Omega_j$ so that $\partial\Omega = \bigcup_{j=1}^{M} \partial\Omega_j$. On each boundary edge $\partial\Omega_j$, we precalculate midpoints, unit normal vectors and associate either Neumann or Dirichlet boundary conditions (others such as Robin can be incorporated too). In addition, we calculate R_0, the radius of the smallest circle centered at the origin that encloses all targets (see Fig. 4(b)).

A frequent and potentially expensive operation is the determination of $d(\mathbf{x}_0, \partial\Omega)$, the distance of $\mathbf{x}_0 \in \mathbb{R}^2 \setminus \Omega$ to the nearest target. A simple approach is to calculate the distance of $\mathbf{x}_0$ to each vertex of $\partial\Omega$ and select the minimum. However, for highly refined target geometries or numerous targets, the number of vertexes to scan over may be prohibitive.

To accommodate such scenarios, we employ a *quadtree*, a common data structure in computational graphics [13]. This structure consists of a hierarchy of Cartesian grids that envelop $\partial\Omega$. At the coarsest level, the bounding box of the target is subdivided into 4 cells. Any cell that contains one or more boundary points is

subdivided into 4 sub-cells, thereby creating the next branch in the tree. This process continues until each cell contains exactly one point, or a predetermined number of levels is used (see Fig. 3).

To determine the closest pointwise distance, the method first queries the midpoints of the coarsest grid and uses simple geometric criteria to eliminate those that cannot contain the closest point. Queries are made of remaining subgrids at the next level of refinement until a predefined level of refinement or a single point remains. This results in a vastly smaller set of candidate vertexes to calculate pointwise distances at the cost of some overheard and extends this approach to large and complex targets sets.
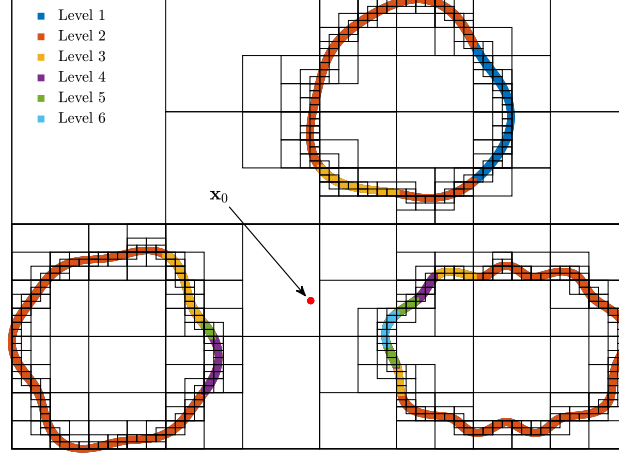

FIG. 3. *Visualization of the quadtree structure method for efficient evaluation of the distance $d(\mathbf{x}_0, \partial\Omega)$. The coloring of each point indicates the highest grid level that the vertex of $\partial\Omega$ is considered for the closest point evaluation. If the maximum refinement level is k, then all points in levels $1, 2, \ldots, k-1$ are excluded from the distance calculation of $d(\mathbf{x}_0, \partial\Omega)$.*

With this setup in place, for each free particle $\mathbf{x}_0 \in \mathbb{R}^2 \setminus \Omega$, we calculate the shortest distance $R = d(\mathbf{x}_0, \partial\Omega)$ and the associated projection $\mathbf{p} = \mathrm{proj}_{\mathcal{P}_j} \mathbf{x}_0$ where $\mathcal{P}_j$ is the line that contains the closest edge $\partial\Omega_j$. The position of the particle is advanced based on four projection steps (Fig. 4) described below.

Stage I: Radially symmetric projector. If $R \in (R_{\min}, R_{\max})$ such that the particle is neither too close nor too far from a target, we project to a ball of radius R centered at $\mathbf{x}_0$. The parameters $R_{\min}, R_{\max}$ are associated with stages II and III respectively and defined shortly. The time duration of this projection step is determined from the solution of the radial diffusion equation with a zero Dirichlet boundary condition at $r = R$ and a Dirac initial condition specifying the particle is initially at the origin. The solution $u(r, t)$ of the parabolic equation

$$\frac{\partial u}{\partial t} = D \frac{1}{r} \frac{\partial}{\partial r} \left(r \frac{\partial u}{\partial r} \right), \quad r \in (0, R), \quad t > 0; \qquad u(R, t) = 0, \quad t > 0; \qquad u(r, 0) = \frac{\delta(r)}{r}, \quad r \in (0, R),$$

gives the cumulative distribution of arrival times at $r = R$ to be

$$(4.29) \qquad F(\tau) = 1 - 2 \sum_{n=0}^{\infty} \frac{e^{-z_n^2 \tau}}{z_n J_1(z_n)}, \qquad t = \frac{D}{R^2} \tau, \qquad J_0(z_n) = 0, \quad n = 0, 1, 2, \ldots.$$

This distribution is sampled by drawing a uniform number $U \in (0, 1)$ and solving $F(\tau) = U$. The CDF $F(\tau)$ is efficiently sampled by precomputing values of z_n and $J_1(z_n)$ and using only as many terms as is necessary to approximate $F(\tau)$ to a predetermined tolerance.
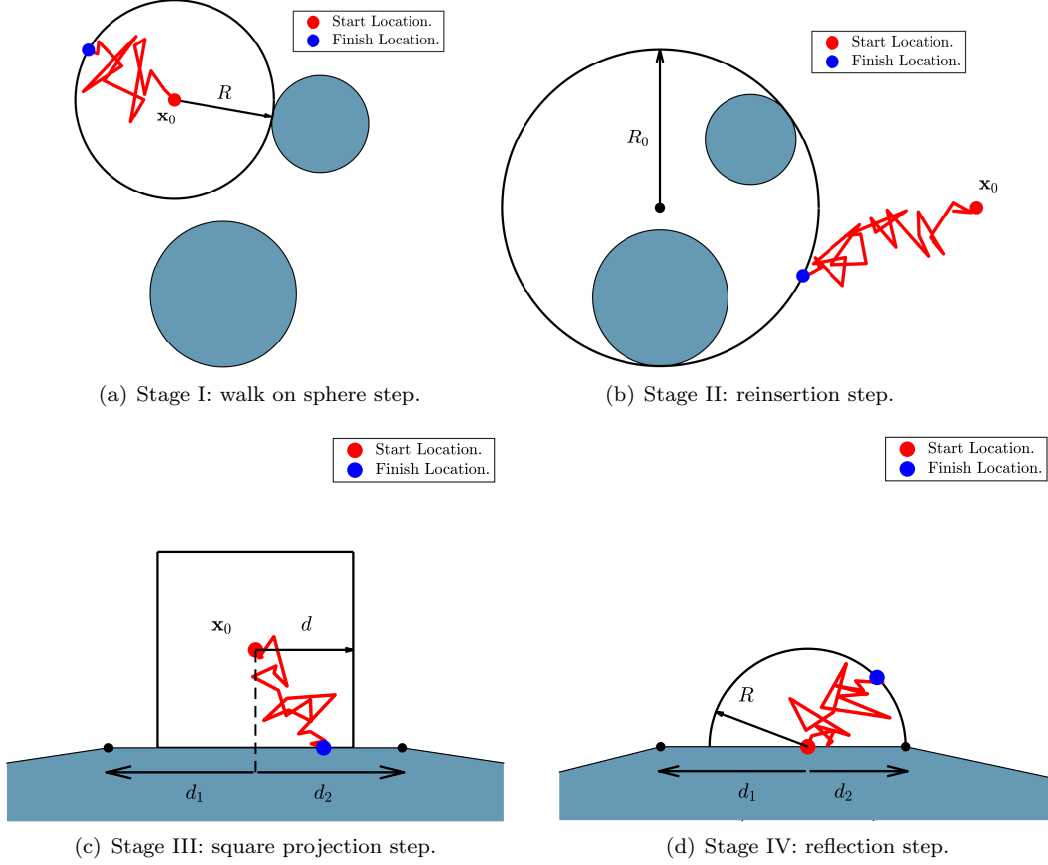
(a) Stage I: walk on sphere step.

(b) Stage II: reinsertion step.

(c) Stage III: square projection step.

(d) Stage IV: reflection step.

FIG. 4. *Schematic of the four stages of the planar KMC algorithm.*

Stage I (alternative for convex shapes): Plane projector. This projector can be adopted when the target is strictly convex so that the entire absorbing target lies to one side of the tangent plane to the surface. After translating the projection point $\mathbf{p}$ to the origin and rotating by the slope of the incident edge, the projection step arises from the solution to the heat equation in the upper half plane with initial location $(0, y_0)$. Combining the relevant fundamental solutions with method of images yields the density

$$u(x, y, t) = \frac{1}{4\pi Dt} \left[e^{-\frac{x^2 + (y - y_0)^2}{4Dt}} - e^{-\frac{x^2 + (y + y_0)^2}{4Dt}} \right],$$

with association arrival time distribution to the plane

$$\rho_T(t) = \int_{\mathbb{R}} u_y(x, 0, t) \, \mathrm{d}x = \frac{y_0}{2\sqrt{\pi}(Dt)^{\frac{3}{2}}} e^{-\frac{y_0^2}{4Dt}}.$$

The cumulative distribution is $\int_0^t \rho_T(\tau) \, \mathrm{d}\tau = \mathrm{erfc}(y_0/\sqrt{4Dt})$ so that the arrival time is sampled as

$$(4.30a) \qquad t_* = \frac{1}{4D} \left[\frac{y_0}{\mathrm{erfc}^{-1}(\eta)} \right]^2, \qquad \eta \in (0, 1).$$

The hitting location on the tangent line is determined by the displacement x_* from the projection point $\mathbf{p}$ which has the (Gaussian) distribution

$$(4.30b) \qquad P_X(x_*) = \frac{u_y(x_*, 0, t_*)}{\rho_T(t_*)} = \frac{1}{\sqrt{4\pi Dt_*}} e^{-\frac{x_*^2}{4Dt_*}},$$

so that $x_* \sim \mathcal{N}(0, 2Dt_*)$.

Stage II: Reinsertion. It is inefficient to simulate the detailed trajectory of particles far from the absorbers. Therefore, when the distance $R = d(\mathbf{x}_0, \partial\Omega)$ exceeds a threshold ($R > R_{\max}$), we project the particle to a smaller disc of radius $R_{\text{ins}} > R_0$ that encloses all the absorbers (Fig. 4(b)). Similar reinsertion procedures have been utilized in Monte Carlo solutions of elliptic problems [15, 18]. Here we must take additional care to sample both the reinsertion time and the time dependent reinsertion location correctly. The arrival distribution for a particle initially on the x-axis (see Appendix A) is

$$(4.31\text{a}) \qquad \mathcal{J}(\tau, \theta) = \frac{D}{R_{\text{ins}}^2} \left[\frac{1}{2\pi} \chi_0(\tau) + \frac{1}{\pi} \sum_{n=1}^{\infty} \chi_n(\tau) \cos n\theta \right], \qquad \theta \in (-\pi, \pi), \quad t > 0, \quad \tau = \frac{D}{R_{\text{ins}}^2} t,$$

where the coefficients are

$$(4.31\text{b}) \qquad \chi_n(\tau) = \frac{2}{\pi} \int_0^\infty \left[\frac{J_n(\omega) Y_n(\omega\mu) - J_n(\omega\mu) Y_n(\omega)}{Y_n^2(\omega) + J_n^2(\omega)} \right] \omega e^{-\omega^2 \tau} \, d\omega.$$

Here $\mu := |\mathbf{x}_0|/R_{\text{ins}}$ is the ratio of the distance $|\mathbf{x}_0|$ of the initial location from the origin to the reinsertion radius R_{ins}. The optimal reinsertion radius is $R_{\text{ins}} = R_0$ where R_0 is the radius of the smallest disc enclosing all absorbers as shown in Fig. 4(b). However, many computational efficiencies are gained by sampling (4.31) for a fixed value of μ - in practice we take $\mu = 60$, $R_{\max} = \mu R_0$ and reinsert to the disc of radius $R_{\text{ins}} = |\mathbf{x}_0|/\mu$. By fixing μ, the integrands of (4.31b) can be tabulated over a range of ω values for efficient quadrature.

The first step in the sampling of (4.31) is to determine the arrival time density $\int_{\theta=0}^{2\pi} \mathcal{J}(\tau, \theta) \, d\theta = \frac{D}{R_{\text{ins}}^2} \chi_0(\tau)$ with associated CDF $F_T(t) = \int_0^\tau \chi_0(\eta) \, d\eta$ where $\tau = \frac{D}{R_{\text{ins}}^2} t$. The arrival time is sampled first since the location will be dependent on this value—for shorter times the arrival location is more tightly focussed around the initial location while for larger arrival times, the insertion location has a weaker dependence on the start location and approaches a uniform distribution (see Fig. 5(b)). For smaller values of τ (in practice $\tau < 10^{10}$), the values of the integrand (4.31b) and the associated CDF are tabulated over a range of ω values for rapid quadrature. The sampling of $\chi_0(\tau)$ can be quite delicate for large τ due to the slow convergence of the integral. To see this, consider that for $\tau \gg 1$ the main contribution to the integral $\chi_0(\tau)$ is when $\omega^2 \tau = \mathcal{O}(1)$ or $\omega \ll 1$. In this regime we have that,

$$(4.32) \qquad \chi_0(\tau) \sim \frac{4 \log \mu}{\pi^2} \int_0^\infty \frac{w}{1 + \frac{4}{\pi^2}(\gamma_e + \log(w/2))^2} e^{-\omega^2 \tau} \, d\omega = \mathcal{O}\left(\frac{1}{\tau |\log \tau|^2} \right), \qquad \tau \to \infty.$$

When $\tau \gg 1$ (in practice $\tau > 10^{10}$), we use the limiting form (4.32) to posit the following explicit form of the density

$$\chi_0(\tau) = \frac{4 \log \mu}{\pi^2} \frac{1}{\tau(a_1 + a_2 \log \tau + a_3 \log \tau^2)} + \mathcal{O}\left(\frac{1}{\tau^2} \right), \qquad \tau \gg 1,$$

for constants a_1, a_2, a_3 determined from fitting. This gives the exact cumulative density function for $\tau \gg 1$

$$(4.33) \quad F_T(t) = 1 - \int_\tau^\infty \chi_0(\eta) \, d\eta = 1 - \frac{4 \log \mu}{\pi^2 \sqrt{4 a_1 a_3 - a_2^2}} \left(\pi - 2 \tan^{-1} \left[\frac{a_2 + 2 a_3 \log \tau}{\sqrt{4 a_1 a_3 - a_2^2}} \right] \right), \qquad \tau = \frac{D}{R_{\text{ins}}^2} t,$$

where for $\mu = 60$, we obtain from fitting the constants

$$a_1 = 1.4670, \qquad a_2 = 0.3102, \qquad a_3 = 0.2029.$$

For a particular arrival time realization $\tau = \tau_*$, the angular location θ of reinsertion satisfies

(a) Arrival time distribution.

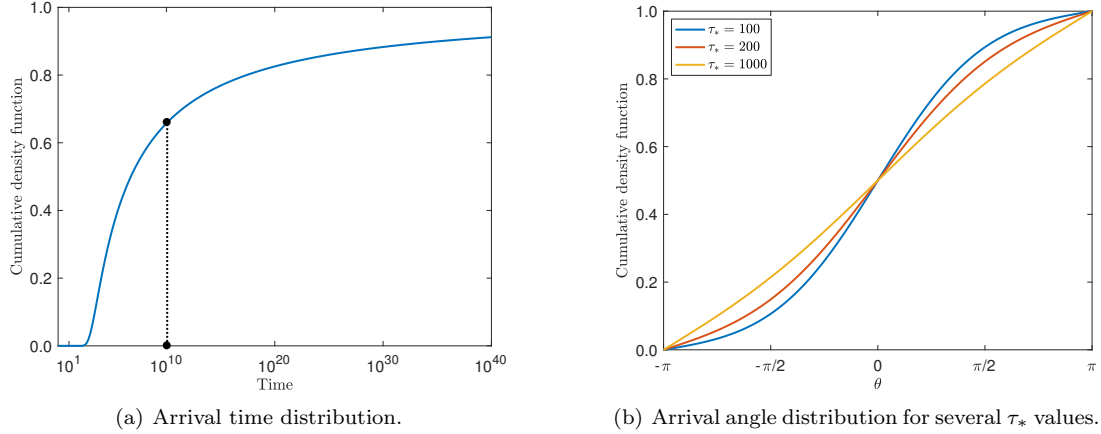(b) Arrival angle distribution for several τ_* values.

FIG. 5. *CDFs of arrival time and location for the reinsertion step when $D = 1$, $\mu = 60$. Left: The reinsertion time distribution $F_\theta(\tau) = \int_0^\tau \chi_0(\eta)\, d\eta$ given by (1.2) (dashed line indicates the cutoff $\tau = 10^{10}$ after which the fitted density (4.33) is used). Right: The arrival location CDF (4.34) for several arrival times τ_*. The distribution is largely uniform for large τ_*.*

$$(4.34) \qquad F_\theta(\theta; \tau_*) = \int_{-\pi}^{\theta} \frac{\mathcal{J}(\tau_*, \eta)}{\chi_0(\tau_*)}\, d\eta = \frac{\theta + \pi}{2\pi} + \frac{1}{\pi} \sum_{n=1}^{\infty} \frac{\sin(n\theta)}{n} \frac{\chi_n(\tau_*)}{\chi_0(\tau_*)}, \qquad \theta \in (-\pi, \pi).$$

To sample from (4.34), a uniform number $U \in (0, 1)$ is drawn and the equation $F_\theta(\theta; \tau_*) = U$ solved for θ. In practice we use an adaptive procedure where we retain only the terms satisfying $|\chi_n(\tau_*)/(n\chi_0(\tau_*))| > \tau_{\mathrm{tol}}$ in the summation of (4.34). For a large proportion of realizations, the arrival time τ_* is sufficiently large (in practice $\tau_* > 10^{10}$) so that the first term is negligible and the arrival location is uniformly distributed on the disc. In Fig. 5, we plot the CDFs of arrival time distribution and arrival location distribution for $\mu = 60$. This method permits rapid and accurate sampling of the reinsertion step.

Stage III: Square projector. If $R < R_{\mathrm{min}}$, then the particle is close enough to determine if contact occurs. By "close enough", we mean that the projection $\mathbf{p}$ lies within the edge segment so that a square of side length $2R$ centered at $\mathbf{x}_0$ lies entirely within the target edge (cf. Fig. 4(c)). This gives explicitly that $R_{\mathrm{min}} = \min(d_1, d_2)$ where d_1, d_2 are the distances between $\mathbf{p}$ and the edge vertexes (cf. Fig. 4(c)). The projection step is then determined from the solution to the parabolic equation on the square $\mathcal{S} = [-R, R]^2$

$$(4.35a) \qquad \frac{\partial u}{\partial t} = D\left(\frac{\partial^2 u}{\partial x^2} + \frac{\partial^2 u}{\partial y^2}\right), \quad \mathbf{x} \in \mathcal{S}, \quad t > 0; \quad u(\mathbf{x}, t) = 0, \quad \mathbf{x} \in \partial\mathcal{S}, \quad t > 0;$$

$$(4.35b) \qquad u(\mathbf{x}, 0) = \delta(x)\delta(y), \quad \mathbf{x} \in \mathcal{S}, \quad t = 0.$$

The separable solution to (4.35) yields the CDF of first arrival times to the square edge $\partial\mathcal{S}$

$$P_T(\tau) = \int_0^\tau \rho_T(\eta)\, d\eta = 1 - \frac{32}{\pi^2} \sum_{l=0}^{\infty} \sum_{k=0}^{\infty} \frac{2k+1}{2l+1} \frac{(-1)^{l+k}}{(2k+1)^2 + (2l+1)^2} e^{-((2l+1)^2 + (2k+1)^2)\pi^2\tau}. \quad \tau = \frac{D}{R^2} t.$$

This distribution is sampled by drawing a uniform number $U \in (0, 1)$ and solving $P_T(\tau^*) = U$. Each side of the square has an equal probability $1/4$ of being hit and the arrival location is sampled from the density

$$\rho_X(x) = \frac{4u_y(x, 0, \tau^*)}{\rho_T(\tau^*)} = \frac{\pi}{2} \frac{\sum_{l=0}^{\infty} \sum_{k=0}^{\infty} (2l+1)(-1)^{l+k} e^{-((2l+1)^2 + (2k+1)^2)\pi^2\tau^*} \sin[(2k+1)\pi x]}{\sum_{l=0}^{\infty} \sum_{k=0}^{\infty} \frac{2k+1}{2l+1} (-1)^{l+k} e^{-((2l+1)^2 + (2k+1)^2)\pi^2\tau^*}}.$$

In practice, we sample with replacement from 10^5 precalculated pairs $\{(\tau_j, x_j)\}$. Further samples can obtained from interpolation on this set.

Stage IV: Reflection step. In the scenario that the particle hits a reflecting portion of the target surface, it is then projected back into the bulk onto a semi-circle of radius $R = \min(d_1, d_2)$, corresponding to the distance to the nearest vertex. In practice, we avoid rounding errors by setting $R = \max(\epsilon, \min(d_1, d_2))$ where ϵ is a small number comparable to machine precision. In the reflecting boundary condition scenario, the projection step is identical to that of stage I with uniform location and arrival time sampled from (4.29). For highly convoluted geometries, it may be that this semi-circle intersects with distal elements of the target. This scenario can be accounted for by calculating the shortest distance d to other segments of the boundary and setting $R = \max(\epsilon, \min(d_1, d_2, d))$.

4.2. Rudimentary convergence analysis in half plane case. In this section we present some analysis of the convergence properties of the KMC approach in the simplified scenario of diffusion in the upper half plane with capture in the window $\{(x, 0) \mid |x| < h/2\}$ with particular emphasis on the role of reinsertion. Specifically, we solve the equation

$$(4.36a) \qquad \frac{\partial u}{\partial t} = \frac{\partial^2 u}{\partial x^2} + \frac{\partial^2 u}{\partial y^2}, \quad x \in \mathbb{R}, \quad y > 0, \quad t > 0;$$

$$(4.36b) \qquad u = 1, \quad y = 0, \quad |x| < \frac{h}{2}, \qquad u_y = 0, \quad y = 0, \quad |x| \geq \frac{h}{2};$$

$$(4.36c) \qquad u = \delta(x - x_0)\delta(y - y_0), \quad x \in \mathbb{R}, \quad y > 0, \quad t = 0.$$

with a simplified KMC method composed of Stages 1(alternative) and 3. From an initial point $\mathbf{x}_0 = (x_0, y_0)$, this algorithm results in a sequence of points $(\mathbf{x}_1, \mathbf{x}_2, \ldots, \mathbf{x}_n) \in \mathbb{R}^{2+}$ which will eventually alight on the absorbing portion. For an ensemble of particles, we denote a_n to be the fraction free after n iterations so

$$a_{n+1} = (1 - p_n)a_n, \qquad a_0 = 1,$$

where p_n is the probability of capture at the nth iteration. To investigate p_n, we first consider the splitting problem $p(x, y)$ for the probability that a particle starting at (x, y) first contacts the plane $y = 0$ on the absorbing window. This satisfies

$$(4.37a) \qquad \frac{\partial^2 p}{\partial x^2} + \frac{\partial^2 p}{\partial y^2} = 0, \quad x \in \mathbb{R}, \quad y > 0;$$

$$(4.37b) \qquad p = 1, \quad y = 0, \quad |x| < h/2, \qquad p = 0, \quad y = 0, \quad |x| \geq h/2,$$

and admits the solution

$$(4.37c) \qquad p(x, y) = \frac{1}{\pi}\left[\tan^{-1}\left(\frac{x + \frac{h}{2}}{y}\right) - \tan^{-1}\left(\frac{x - \frac{h}{2}}{y}\right)\right].$$

We consider that the current location $\mathbf{x}_n = (x_n, y_n)$ has arisen from a projection step (stage III). Without loss of generality, we assume the previous contact $(\bar{x}_n, 0)$ with the $y_n = 0$ plane is such that $\bar{x}_n > \frac{h}{2}$. We may then parameterize (cf. Fig. 6) the point $\mathbf{x}_n = (x_n, y_n)$ as

$$x_n = \frac{h}{2} + \bar{r}_n(1 + \cos\phi), \qquad y_n = \bar{r}_n \sin\phi, \qquad \phi \in (0, \pi), \qquad \bar{x} \in (h/2, \infty).$$
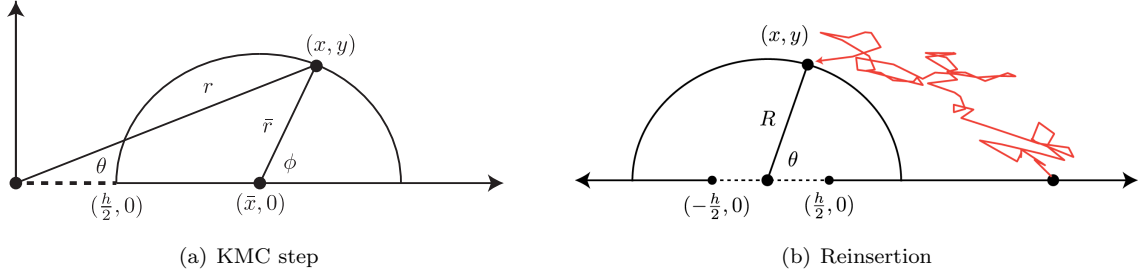
(a) KMC step   (b) Reinsertion

FIG. 6. *A schematic showing the simplified KMC solution in the upper half place. (a) the projection step from the real line back into the bulk. (b) The reinsertion step to keep the particle in the vicinity of the absorbing set.*

It follows from the splitting probability (4.37c) that

$$p(x_n, y_n) = \frac{1}{\pi} \left[\tan^{-1} \left(\frac{x_n - \frac{h}{2}}{y_n} + \frac{h}{y_n} \right) - \tan^{-1} \left(\frac{x_n - \frac{h}{2}}{y_n} \right) \right]$$

$$= \frac{1}{\pi} \left[\tan^{-1} \left(\cot \frac{\phi}{2} + \frac{h}{\bar{r}_n} \csc \phi \right) - \tan^{-1} \left(\cot \frac{\phi}{2} \right) \right]$$

$$= \frac{1}{\pi} \left[\tan^{-1} \left(\tan \left(\frac{\pi}{2} - \frac{\phi}{2} \right) + \frac{h}{\bar{r}_n} \csc \phi \right) - \left(\frac{\pi}{2} - \frac{\phi}{2} \right) \right],$$

where the angles $\phi \in (0, \pi)$ are distributed uniformly. Applying the change of variables $\eta = \frac{\pi - \phi}{2}$ yields

$$p = \frac{1}{\pi} \left[\tan^{-1} \left(\tan \eta + \alpha_n \csc 2\eta \right) - \eta \right], \qquad \alpha_n = \frac{h}{\bar{r}_n}.$$

We now define the average probability $p_n = \frac{1}{\pi} \int_{\phi=0}^{\pi} p \, d\phi = \frac{2}{\pi} \int_{\eta=0}^{\pi/2} p \, d\eta$ and find that

$$(4.38) \qquad p_n = \frac{2}{\pi^2} \int_{\eta=0}^{\frac{\pi}{2}} \left[\tan^{-1} \left(\tan \eta + \alpha_n \csc 2\eta \right) - \eta \right] d\eta, \qquad \alpha_n = \frac{h}{\bar{r}_n}.$$

Without reinsertion, many trajectories will yield very small values for the parameter α_n as $\bar{r}_n$ can attain very large values. To gain further insight into this scenario, we consider the limiting case of (4.38) as $\alpha \to 0$.

4.3. Asymptotic analysis of splitting probability. Here we develop an asymptotic approximation for (4.38) in the limit as $\alpha \to 0$ (subscript n dropped for convenience). The integral features global contributions and local contributions near $\eta = 0$. To delineate between these contributions, we define the small parameter $\delta > 0$ such that $\alpha \ll \delta \ll 1$. Then we have that

$$(4.39) \qquad p_n(\alpha) = \underbrace{\frac{2}{\pi^2} \int_{\eta=0}^{\delta} \left[\tan^{-1} \left(\tan \eta + \alpha \csc 2\eta \right) - \eta \right] d\eta}_{A_1} + \underbrace{\frac{2}{\pi^2} \int_{\eta=\delta}^{\frac{\pi}{2}} \left[\tan^{-1} \left(\tan \eta + \alpha \csc 2\eta \right) - \eta \right] d\eta}_{A_2}.$$

where A_1 and A_2 will be considered separately and combined so that their sum is independent of δ.

Evaluation of A_1. In this region we apply the approximation $\tan^{-1}(x+y) = \tan^{-1}(x) + y/(1+x^2) + \mathcal{O}(y^2)$ for $y \to 0$ with $x = \alpha \csc 2\eta$ and $y = \tan \eta$. Then we have that

$$A_1 := \frac{2}{\pi^2} \int_0^{\delta} \left[\tan^{-1} \left(\tan \eta + \alpha \csc 2\eta \right) - \eta \right] d\eta \sim \frac{2}{\pi^2} \int_0^{\delta} \left[\tan^{-1}(\alpha \csc 2\eta) + \frac{\tan \eta}{1 + \alpha^2 \csc^2(2\eta)} - \eta \right] d\eta.$$

Applying small argument approximations for $\eta \ll 1$, we have that

$$A_1 \sim \frac{2}{\pi^2} \int_0^\delta \left(\tan^{-1}\left(\frac{\alpha}{2\eta}\right) - \frac{\alpha^2 \eta}{4\eta^2 + \alpha^2} \right) d\eta = \frac{\alpha}{\pi^2} \int_0^{\frac{2\delta}{\alpha}} \left(\tan^{-1}\frac{1}{z} - \frac{\alpha}{2}\frac{z}{z^2+1} \right) dz, \qquad (\eta = \alpha z/2)$$

$$= \frac{\alpha}{\pi^2} \left[\frac{1}{2}\log(1+z^2) + z\tan^{-1}\frac{1}{z} - \frac{\alpha}{4}\log(1+z^2) \right]_0^{\frac{2\delta}{\alpha}} = \frac{\alpha}{\pi^2} \left[\left(\frac{1}{2} - \frac{\alpha}{4} \right) \log\left(1 + \frac{4\delta^2}{\alpha^2} \right) + \frac{2\delta}{\alpha}\tan^{-1}\frac{\alpha}{2\delta} \right].$$

The parameter δ is defined so that $\alpha \ll \delta$ and therefore $\frac{\delta}{\alpha} \gg 1$. Applying Taylor we find that

$$(4.40) \qquad\qquad A_1 = \frac{\alpha}{\pi^2} \left(\log\frac{2\delta}{\alpha} + 1 \right) + \mathcal{O}\left(\frac{\alpha^3}{\delta^2}, \alpha^2 \log\left(\frac{\delta}{\varepsilon}\right) \right).$$

Evaluation of A_2. In the integral A_2 we have that $\alpha \ll \delta$ and apply the approximation $\tan^{-1}(x+y) = \tan^{-1}(x) + y/(1+x^2) + \mathcal{O}(y^2)$ for $y \to 0$ with $x = \tan\eta$ and $y = \alpha\csc 2\eta$. It then follows that

$$A_2 := \frac{2}{\pi^2} \int_{\eta=\delta}^{\frac{\pi}{2}} \left[\tan^{-1}(\tan\eta + \alpha\csc 2\eta) - \eta \right] d\eta \sim \frac{2}{\pi^2} \int_\delta^{\frac{\pi}{2}} \left[\tan^{-1}(\tan\eta) + \alpha\frac{\csc 2\eta}{1 + \tan^2\eta} - \eta \right] d\eta$$

$$= \frac{2\alpha}{\pi^2} \int_\delta^{\frac{\pi}{2}} \frac{\csc 2\eta}{1 + \tan^2\eta} d\eta = \frac{\alpha}{\pi^2} \int_\delta^{\frac{\pi}{2}} \cot\eta\, d\eta = \frac{\alpha}{\pi^2} [\log\sin\eta]_\delta^{\frac{\pi}{2}}$$

$$(4.41) \qquad = -\frac{\alpha}{\pi^2}\log\delta.$$

To finalize the approximation of (4.39), we combine expressions (4.40) and (4.41) and reintroduce α_n reflecting that this parameter changes over each iteration. This yields that

$$(4.42) \qquad\qquad p_n \sim A_1 + A_2 = \frac{\alpha_n}{\pi^2} \left(\log\frac{2}{\alpha_n} + 1 \right), \qquad \alpha_n \to 0, \qquad \alpha_n = \frac{h}{\bar{r}_n}.$$

Hence we see that while the probability of capture is positive at each iteration, it can become arbitrarily small as $|\bar{x}_n| = \frac{h}{2} + \bar{r}_n \to \infty$. This results in an algorithm with polynomial convergence rate (see Fig. 8(a)). A comparison of the asymptotic approximation (4.42) with (4.38) is displayed in Fig. 7(a).

4.4. Reinsertion analysis. The aim of reinsertion is to reestablish exponential convergence rate in the algorithm by limiting the maximum value of $\bar{x}_n$ and hence promoting faster capture.

Reinsertion projects wayward particles back to a smaller disc of radius R that encloses all targets and therefore omits simulating trajectories far from the capture regions. When reinserting from sufficiently distant points, the placement on the disc is largely uniform with $(x, y) = R(\cos\theta, \sin\theta)$ with small corrections given by (4.34). Points on this disk have average probability of capture (see (4.37))

$$p_n = \frac{1}{\pi} \int_0^\pi p(R\cos\theta, R\sin\theta)\, d\theta = \frac{1}{\pi^2} \int_0^\pi \left[\tan^{-1}\left(\cot\theta + \frac{h}{2R}\csc\theta \right) - \tan^{-1}\left(\cot\theta - \frac{h}{2R}\csc\theta \right) \right] d\theta$$

$$(4.43) \qquad \sim \frac{2}{\pi^2}\frac{h}{R}, \quad \text{as} \quad \frac{h}{R} \to 0.$$

The accuracy of the approximation (4.43) is shown in Fig. 7(b). In an ensemble of particles, some will be reinserted to the disk $x^2 + y^2 = R^2$ while others remain inside it. Those inside have greater probability of capture at the next step, therefore the quantity (4.43) reflects a lower bound on the likelihood of capture. Hence we see that the probability of capture after n stages has bound $p_n \gtrsim \frac{2}{\pi^2}\frac{h}{R}$. The key observation here

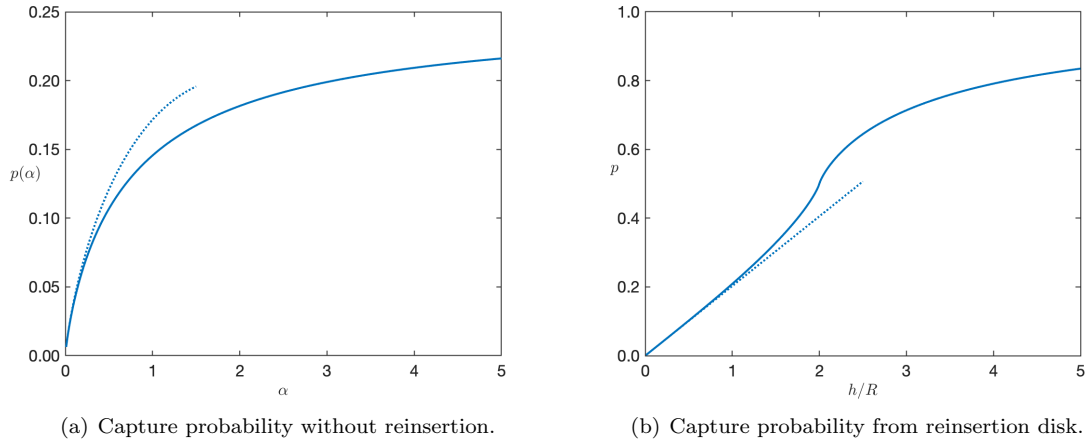(a) Capture probability without reinsertion. (b) Capture probability from reinsertion disk.

FIG. 7. *(Left figure) Comparison of the capture probability $p_n(\alpha)$ (solid curve) (4.38) and the small arguement approximation (4.42) (dashed curve) without reinsertion. We note that $p \to 1/4$ for $\alpha_n = h/\bar{r}_n \to \infty$. (Right figure) Here we show the probability of capture with reinsertion to a disk of radius R.*

is that the probability of capture at each iteration is now bounded below by a constant defined in term of the geometric parameter h and the reinsertion radius R. This ensures an exponential convergence rate of the algorithm with slower rates associated with smaller targets ($h \ll 1$) and a faster rate associated with a smaller reinsertion radius R.

As an exposition of this analysis, we show in Fig. 8 the convergence of the KMC method on the simplified half plane problem (4.36) with and without reinsertion. In the absence of reinsertion, polynomial convergence is attained as shown by linear behavior on a log-log plot. When reinsertion is implemented (to radius $R = 1$), we observe exponential convergence shown by linear behavior on a log plot. This demonstrates the key role of reinsertion in attaining exponential convergence of the KMC method.
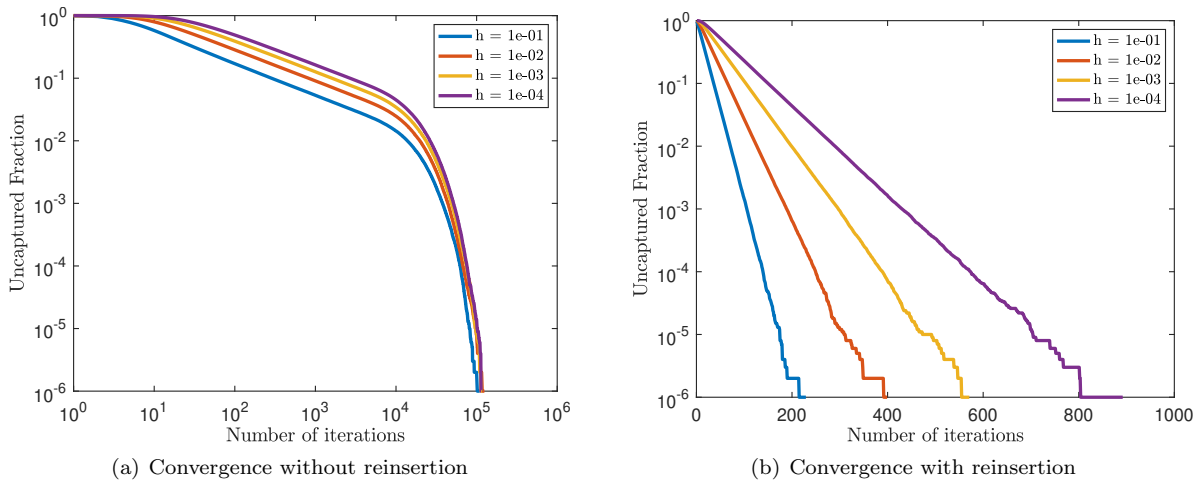

(a) Convergence without reinsertion (b) Convergence with reinsertion

FIG. 8. *Convergence statistics of the KMC method for the simplified problem (4.36). Left: In the absence of reinsertion, a polynomial rate of convergence is attained shown by the linear behavior on the log-log plot. Right: Reinsertion recovers exponential convergence as seen in the linear behavior on the log plot. Simulations based on ensemble of 10^6 particles.*

5. Results. In this section we show a variety of examples to demonstrate the ability of these methodologies for approximating full arrival time distributions to complex absorbing sets. In our simulations, we have used a common diffusivity of $D = 1$. Arrival times from the KMC method are translated with $t \to t+1$ so that $t = 0$ is mapped to 10^0 in log space. `MATLAB`'s histogram function is then applied with the "probability" normalization option. The hybrid approaches refer to solving the Laplace transform using either the expansion asymptotic (2.13) or the boundary integral method (BIM) described in Sec. 3. This is followed by numerical inversion of the transform equation as described in Sec. 2.1.

5.1. Planar results. Here we use three examples to validate the numerical KMC method and corroborate with both the hybrid approaches (asymptotic and boundary integral). The first example is a simple one target scenario in which the closed form solution (A.58) is available for comparison. The remaining two examples show the efficacy of the method on more complex absorbing sets consisting of multiple targets of varying radii. The parameter values for the three examples are

(One target) $\mathbf{x}_1 = (0, 0), \quad r_1 = 0.05, \quad \mathbf{x}_0 = (5, 0).$

(Three targets) $\mathbf{x}_1 = (3, 3), \quad \mathbf{x}_2 = (8, 8), \quad \mathbf{x}_3 = (10, 10), \qquad r_1 = \dfrac{1}{8}, \quad r_2 = \dfrac{1}{6}, \quad r_3 = \dfrac{1}{3}, \quad \mathbf{x}_0 = (0, 0).$

(Six targets) $\mathbf{x}_1 = (-3, 0), \quad \mathbf{x}_2 = (0, -2), \quad \mathbf{x}_3 = (\sqrt{2}, -\sqrt{2}), \quad \mathbf{x}_4 = (2, 0),$

$\mathbf{x}_5 = (\sqrt{2}, \sqrt{2}), \quad \mathbf{x}_6 = (0, 2), \qquad r_1 = 0.275, \quad r_2 = \ldots = r_6 = 0.02, \quad \mathbf{x}_0 = (0, 0).$

The results shown in Fig. 9 show good agreement between the three approaches. In Fig. 9(a) we compare the hybrid-asymptotic, KMC and exact one-pore solutions showing excellent agreement. In the two more challenging examples, we generally see good agreement between the asymptotic and boundary integral approaches. In the more challenging 6 target case, we see in Fig. 9(c) a slightly diminished agreement is observed near the peak.
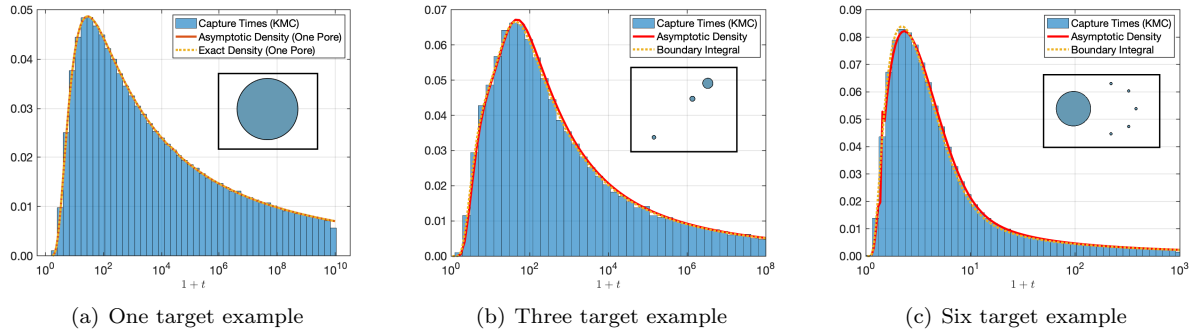

(a) One target example   (b) Three target example   (c) Six target example

FIG. 9. *Relative frequency of arrival times to planar targets from $N = 1 \times 10^6$ KMC arrival times, exact solution (one target case), and hybrid approaches (asymptotic and boundary integral). Schematics of target arrangements shown as insets.*

5.2. Homogenization. In this example, we consider the case of a single target with a mix of absorbing and reflecting portions. This describes the scenario where an impermeable cellular membrane surface is covered in surface receptors. We determine the full distribution of arrival times using both the KMC method and the hybrid asymptotic-homogenization result (2.21). In the application of the hybrid approach, we use

the analytically determined logarithmic capacitance (2.21), or equivalently the effective radius, in the single patch result.
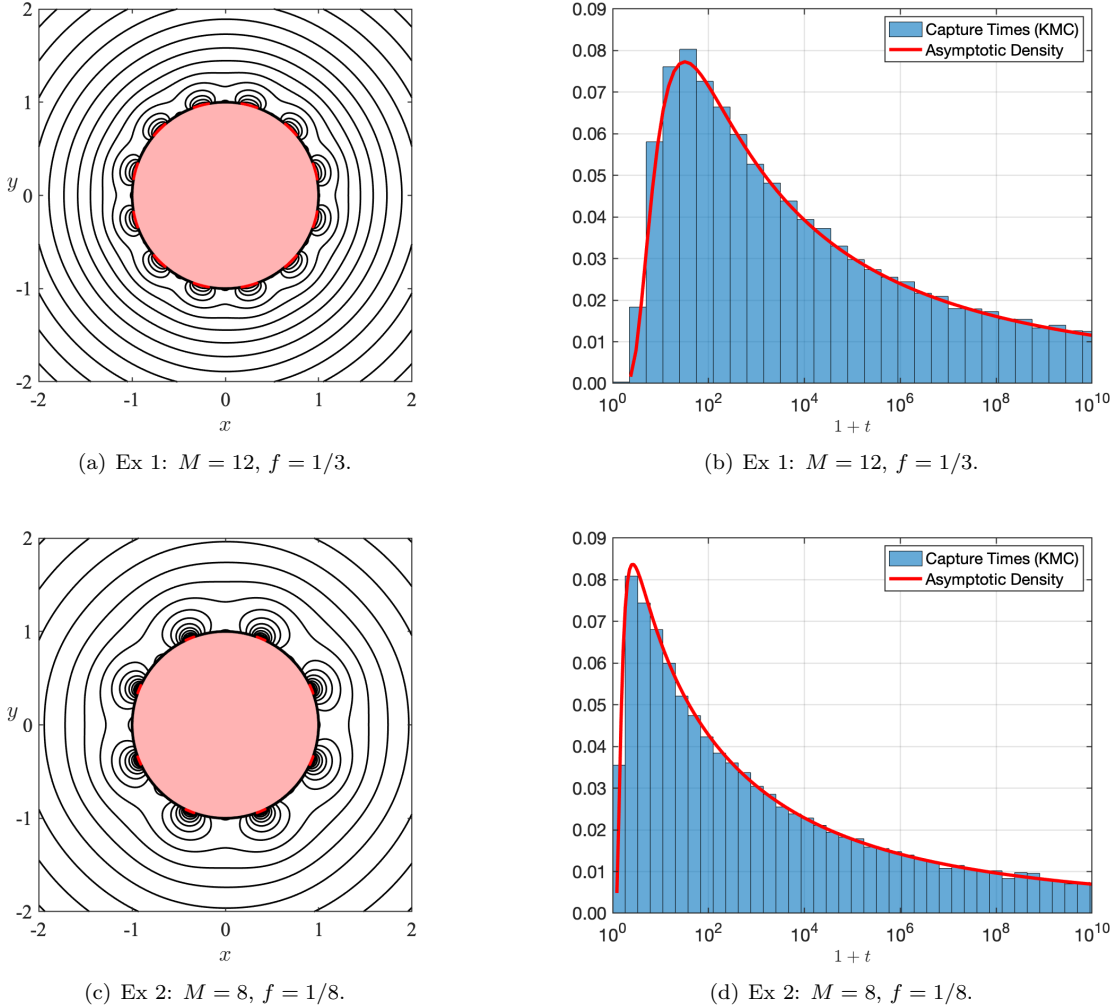

(a) Ex 1: $M = 12$, $f = 1/3$.

(b) Ex 1: $M = 12$, $f = 1/3$.

(c) Ex 2: $M = 8$, $f = 1/8$.

(d) Ex 2: $M = 8$, $f = 1/8$.

FIG. 10. *Results from the KMC and asymptotic method on the homogenization examples (5.44). Left panels: target (scaled to unity radius) with layout of absorbers. Contours indicate the numerical solution of (2.8). Right figures: Agreement between the full arrival time densities obtained from $N = 10^5$ KMC arrival times and the hybrid-asymptotic method.*

In the two examples shown in Fig. 10, we take a circular absorbing target centered at the origin with radius $\varepsilon = 0.05$. The target itself features M equally spaced absorbing windows centered at the roots of unity $(\cos \frac{2\pi k}{M}, \sin \frac{2\pi k}{M})$. The windows occupy a combined fraction f and each has common angular extent $\sigma = \frac{2\pi f}{M}$. In each case we use the homogenized formula (2.21c) to obtain the logarithmic capacitance d and then apply the result (2.14) for $N = 1$.

The relevant parameters obtained for the two examples are

(5.44a)   Ex 1: $M = 12$, $f = \dfrac{1}{3}$, $d = 0.8978$, $\mathbf{x}_0 = [5, 0]$;

(5.44b)   Ex 2: $M = 8$, $f = \dfrac{1}{8}$, $d = 0.6657$, $\mathbf{x}_0 = [2, 0]$.

In Fig. 10(b),(d) we show good agreement between the two methods while in Fig. 10(a),(c) we display a visualization of the solution to the capacitance problem (2.8). We remark that the homogenization effect can be seen through the gradual radial symmetrization of the contours.

5.3. Clustering. In this section, we use two examples of clustered target configurations to compare results from the KMC method with both the asymptotic and BIM approaches. In addition, we show the effectiveness of homogenization where the clustered target configuration is replaced by a single circular target of appropriately chosen radius. The specific parameters are given by

$$(5.45a) \quad \text{Ex 1:} \quad \mathbf{x}_k = \frac{3}{2}\left(\cos\frac{2\pi k}{5}, \sin\frac{2\pi k}{5}\right), \quad k = 1, \dots, 5, \quad \mathbf{x}_6 = (0,0), \quad r_{1,\dots,6} = 0.1, \quad \mathbf{x}_0 = (10,0);$$

$$(5.45b) \quad \text{Ex 2:} \quad \mathbf{x}_k = \frac{3}{2}\left(\cos\frac{2\pi k}{8}, \sin\frac{2\pi k}{8}\right), \quad k = 1, \dots, 8, \quad r_{1,\dots,8} = 0.05, \quad \mathbf{x}_0 = (5,0).$$

(a) Numerical solution of (2.8) yielding logarithmic capacitance $d = 1.2295$.

(b) Normalized target fluxes.

(c) Agreement of capture times (from KMC) with asymptotic and homogenized densities.

(d) Numerical solution of (2.8) yielding logarithmic capacitance $d = 1.2737$.

(e) Normalized target fluxes.

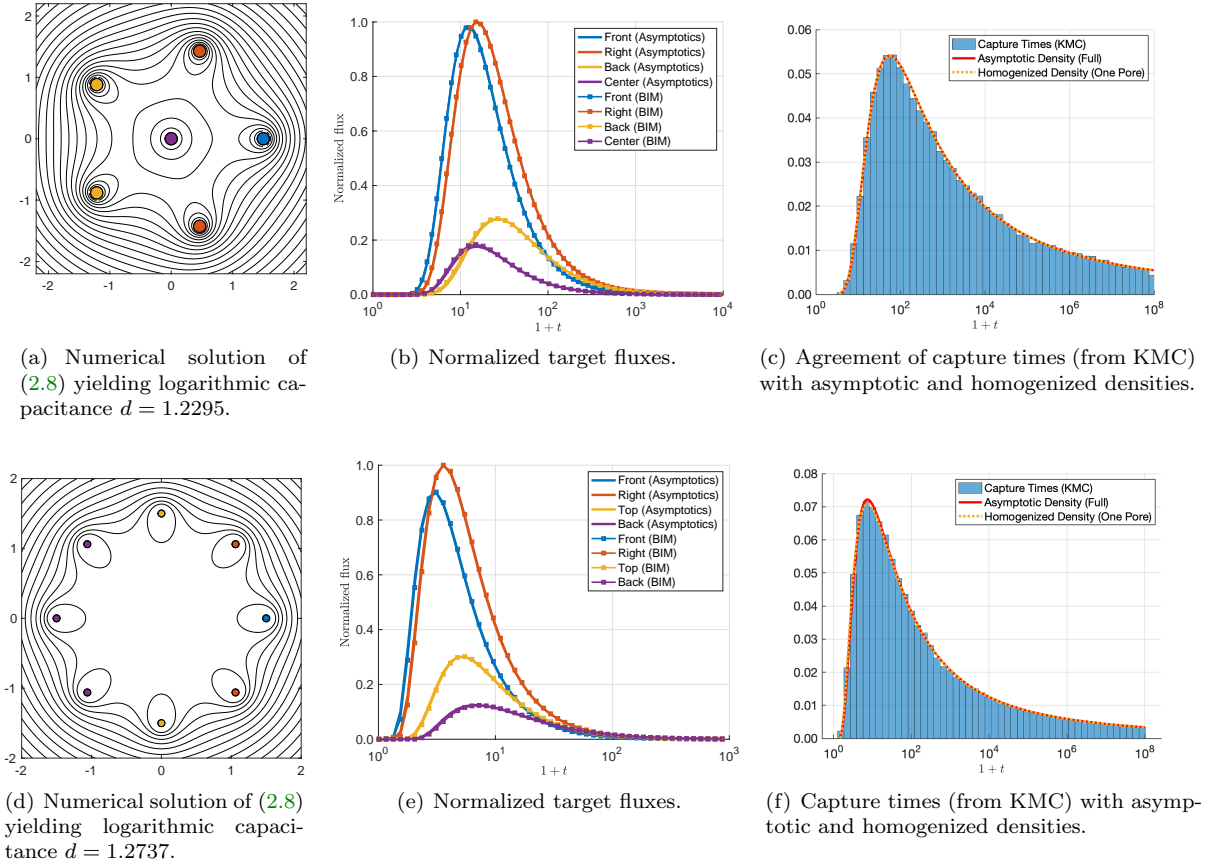(f) Capture times (from KMC) with asymptotic and homogenized densities.

FIG. 11. *Comparison of the full asymptotic density with those arising from the KMC method, boundary integral method (BIM) and homogenization (replacing the target cluster with a single absorbing target). Panels (a,d) display schematics of the target configuration. Panels (b,e) show fluxes over groups of receptors as colored in the schematic. Panels (c,f) favorably compare homogenized and asymptotic densities of to those derived from $N = 10^5$ KMC times.*

The numerical method described by equation (2.23) allows for the computation of the logarithmic capacitance for each of the absorbing sets (cf. Fig. 11(a,d)). For the parameters specified in (5.45), we determine

$d = 1.2295$ (Ex 1) and $d = 1.2737$ (Ex 2). The logarithmic capacitance can be interpreted as the effective radius of a single target that reflects the capture potential of the cluster. As with the homogenization example in Sec 5.2, we observe that replacing complex configurations with a single target of appropriately chosen radius produces a very accurate representation of the full arrival time distribution. However, the single target representation does reduce certain direction information encoded in the distribution of arrivals over the targets in the cluster. The hybrid-asymptotic method can rapidly determine the fluxes by numerical inverse Laplace transform of $\hat{\mathcal{J}}_j = 2\pi D\nu_j S_j$ where each S_j is determined by (2.13). In Fig. 11(b,e) we show normalized fluxes into four sets of traps that are symmetrically arranged with respect to the initial location. The traps aligned towards the initial data accrue most of the inbound flux while the peaks, representing most likely arrival times at a particular target, are ordered by their distance to the initial location. The distribution of fluxes over the targets encode directional information that can infer the source location [25].

5.4. Splitting Probabilities. In this section, we demonstrate the convergence of the dynamic fluxes to the static splitting probabilities $\{\phi_k(\mathbf{x})\}_{k=1}^N$, where $\phi_k(\mathbf{x})$ denotes the probability that a diffusing particle originally at $\mathbf{x}$ reaches the kth target before any others. For exposition purposes, we focus on the scenario of completely absorbing targets. These probabilities satisfy the exterior Laplace problem

$$(5.46a) \qquad \Delta\phi_k = 0, \quad \mathbf{x} \in \mathbb{R}^2 \setminus \Omega; \qquad \phi_k(\mathbf{x}) = \delta_{jk}, \quad \mathbf{x} \in \partial\mathcal{A}_j, \qquad j = 1, \ldots, N;$$

$$(5.46b) \qquad \phi_k(\mathbf{x}) \quad \text{finite as} \quad |\mathbf{x}| \to \infty,$$

where δ_{jk} is the Kronecker delta. The asymptotic solution of (5.46) as $\varepsilon \to 0$ is developed along similar lines to Sec. 2 (also see [24, Sec 5]). Accordingly, we present the solution as $\varepsilon \to 0$ directly as

$$(5.47a) \qquad \phi_k(\mathbf{x}) \sim 2\pi \sum_{j=1}^N \nu_j A_j G_0(\mathbf{x}; \mathbf{x}_j) + \bar{\phi}, \qquad G_0(\mathbf{x}; \mathbf{y}) = \frac{1}{2\pi} \log|\mathbf{x} - \mathbf{y}|,$$

where the $(N+1)$ constants $(A_1, \ldots, A_N, \bar{\phi})$ are determined from the linear system,

$$(5.47b) \qquad \sum_{j=1}^N \nu_j A_j = 0; \qquad -A_j + 2\pi \sum_{\substack{i=1 \\ i \neq j}}^N \nu_i A_i G_0(\mathbf{x}_j; \mathbf{x}_i) + \bar{\phi} = \delta_{jk}, \qquad j = 1, \ldots, N.$$

The gauge functions $\nu_j = -1/\log\varepsilon d_j$ are defined in (2.9). We remark that since capture is guaranteed for planar Brownian motion, we have that $\sum_{k=1}^N \phi_k(\mathbf{x}) = 1$.

To demonstrate this theory, we compare these static splitting probabilities with the time-dependent fractional signals

$$(5.48) \qquad q_k(t) = \frac{\int_0^t \mathcal{J}_k(\eta)d\eta}{\sum_{j=1}^N \int_0^t \mathcal{J}_j(\eta)d\eta}, \qquad k = 1, \ldots, N;$$

into each target (see Fig. 12) obtained from the hybrid-asymptotic method (Sec. 2). We draw attention to two important conclusions from this example. First, the dynamic signal converges to the static splitting probabilities on a very long timescale. For many physically or biologically relevant timescales, this questions the usefulness of using splitting probabilities for inference [25] purposes. Second, the ordering of the relative fluxes into each target changes over the displayed time interval. Specifically, at short times ($t \lessapprox 10^1$), target

(a) Schematic of target configuration.

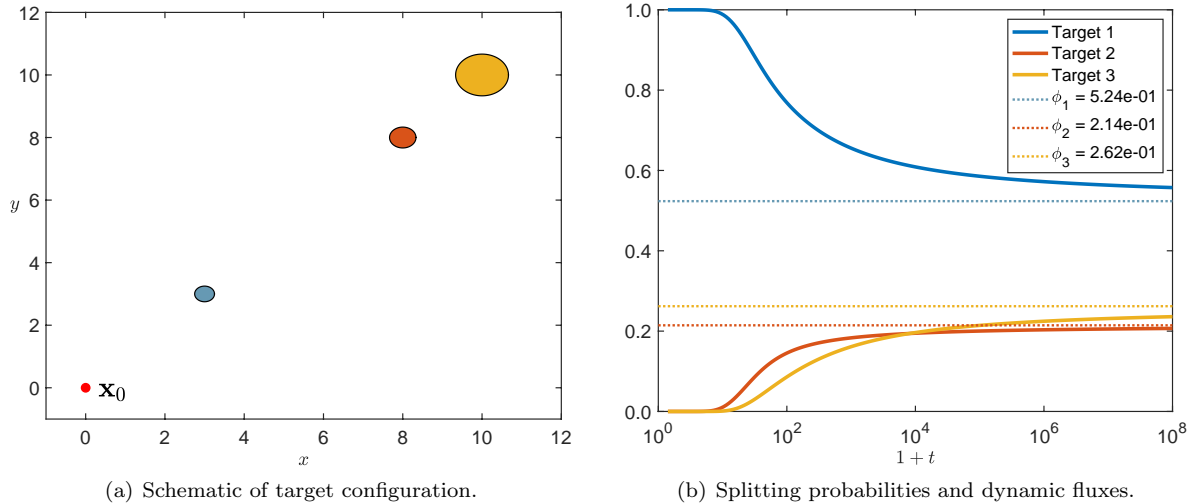(b) Splitting probabilities and dynamic fluxes.

FIG. 12. *Left: A schematic of the three target configuration from Sec. 5.1. Right: The fractional signal $q_k(t)$ (5.48) into each target together with the steady state splitting probabilities ϕ_k obtained from (5.47).*

1 captures almost all the signal and indeed is the most significant absorber over the entire timeline. Target 1 is the smallest target but closest to the initial location demonstrating that this distance is a significant indicator of capture ability. Later in the timeline, we see that targets 2 and 3 interchange their prominence in signal (around $t \approx 10^4$) implying that proximity to the initial location promotes faster capture at short times while at larger times, target size can play a more significant role. Importantly, none of these subtleties are apparent from the static splitting probabilities highlighting the necessity of obtaining full time dependent statistics.

6. Discussion. In this work we have demonstrated several methodologies for obtaining arrival time statistics of diffusing particles to complex sets of absorbing targets in planar regions. The Laplace transform approach seeks to solve an equation of modified Helmholtz type by either an asymptotic expansion for well separated targets or a boundary integral representation. In both cases the target geometries can be very general, but for the boundary integral method, it is presently limited to purely absorbing targets. In future work, we aim to extend to targets with both absorbing and reflecting components. The inverse transform is obtained by quadrature of the Bromwich integral. To complement these approaches, we developed a particle based kinetic Monte-Carlo (KMC) method that can resolve the arrival distribution for very general configurations of targets and boundary sets. These methods are rapid, accurate and easy to implement. The hybrid asymptotic method is particularly suited to the scenario of well-separated targets while the KMC method is applicable to general geometric scenarios and varied boundary conditions.

There are a few conclusions that emerge from our study. Homogenization is a powerful technique that accurately reproduces the first passage time distributions of complex target sets by replacing them with a single circular target of appropriately chosen radius. However, homogenization brings limitations with it, particularly as it coarse grains the spatial distribution of arrivals across the targets. The relative fraction of particles that arrive across a distribution of targets has directional information that can be used to infer source location [25]. Additionally, the dynamics available from the full distribution of arrival statistics
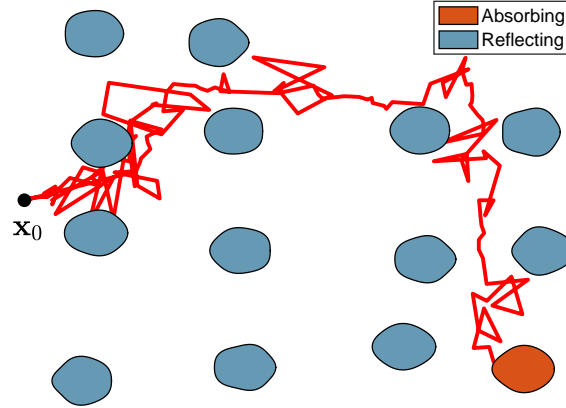
FIG. 13. *A tricky first passage time distribution to evaluate using either KMC or hybrid-asymptotic methods.*

reveals the limitations of using static information, (e.g. splitting probabilities) which are only representative of very long time behavior. Our example of dynamic splitting probabilities (Sec. 5.4) suggests that there are several timescales over which arrival statistics can be important and that the relevant physical or biological timescale must be considered when inferring source location from arrival information. Coarse graining is also unreasonable for non-homogeneous distributions of grains that arise in applications such as microscale erosion [12, 37].

While the methods developed here are quite general, there are certain scenarios where they fail and new approaches are needed. For example, in the scenario where there are numerous targets but only a few are reactive (Fig. 13), particles must navigate a torturous route through inert targets to reach the destination. The combination of targets with either purely Neumann or Dirichlet boundary conditions hampers all the approaches developed here. This scenario is particularly challenging for the KMC method due to the fact that on a reflecting target surface, the particle will tend to perform a surface diffusion characterized by many small jumps. The very long wait time for a large jump necessary to leave the target vicinity means that the convergence rate is greatly reduced. To address these shortcoming, we plan extensions to the boundary integral formulation.

Appendix A. Two dimensional problem arrival problem. Arrival time and angle distribution.

For a particle with diffusivity D originally at $\mathbf{x} \in (b, 0)$, the occupation density in $r = |\mathbf{x}| > a$ satisfies

$$p_t = D\left(p_{rr} + \frac{1}{r}p_r + \frac{1}{r^2}p_{\theta\theta}\right), \qquad r > a, \quad \theta \in (-\pi, \pi), \quad t > 0; \tag{A.49a}$$

$$p(a, \theta, t) = 0, \qquad \theta \in (-\pi, \pi), \quad t > 0; \tag{A.49b}$$

$$p(r, \pi, t) = p(r, -\pi, t), \qquad r > a, \quad t > 0; \tag{A.49c}$$

$$p(r, \theta, 0) = \frac{1}{r}\delta(r - b)\delta(\theta), \qquad r > a, \quad \theta \in (-\pi, \pi). \tag{A.49d}$$

Our goal is to determine closed form expressions for the quantities

$$(A.50a) \qquad P(t) = \int_{\theta=-\pi}^{\pi} \int_{r=a}^{\infty} p(r,\theta,t)\, r dr d\theta, \qquad \text{[Survival probability]}$$

$$(A.50b) \qquad C(t) = 1 - \int_{\theta=-\pi}^{\pi} \int_{r=a}^{\infty} p(r,\theta,t)\, r dr d\theta, \qquad \text{[Capture probability]}$$

$$(A.50c) \qquad S(t) = -P'(t), \qquad \text{[Arrival time distribution]}$$

Applying the divergence theorem to $S(t) = -P'(t)$, we see that

$$(A.51) \qquad S(t) = -\int_{\theta=-\pi}^{\pi}\int_{r=a}^{\infty} p_t(r,\theta,t)\, r dr d\theta = -D\int_{\theta=-\pi}^{\pi}\int_{r=a}^{\infty}(rp_r)_r\, dr d\theta = Da\int_{\theta=-\pi}^{\pi} p_r(a,\theta,t)\, d\theta.$$

To obtain the flux $p_r(a,\theta,t)$, we non-dimensionalize by introducing variables

$$(A.52a) \qquad p(r,t) = \frac{1}{a^2}\tilde{p}(\tilde{r},\theta,\tilde{t}), \qquad \tilde{r} = \frac{1}{a}r, \qquad \tilde{t} = \frac{D}{a^2}t, \qquad R = \frac{b}{a}.$$

so that $S(t) = \frac{D}{a^2}\int_{\theta=-\pi}^{\pi}\tilde{p}_{\tilde{r}}(1,\theta,\tilde{t})\, d\theta$. Under the change of variables (A.52a), (A.49) becomes

$$(A.52b) \qquad \tilde{p}_{\tilde{t}} = \left(\tilde{p}_{\tilde{r}\tilde{r}} + \frac{1}{\tilde{r}}\tilde{p}_{\tilde{r}} + \frac{1}{\tilde{r}^2}\tilde{p}_{\theta\theta}\right), \qquad \tilde{r} > 1, \quad \theta \in (-\pi,\pi), \quad \tilde{t} > 0;$$

$$(A.52c) \qquad \tilde{p}(1,\theta,\tilde{t}) = 0, \qquad \theta \in (-\pi,\pi), \quad \tilde{t} > 0;$$

$$(A.52d) \qquad \tilde{p}(\tilde{r},\theta,0) = \frac{1}{\tilde{r}}\delta(\tilde{r}-R)\delta(\theta), \qquad \tilde{r} > 1, \quad \theta \in (-\pi,\pi).$$

After dropping the tildes, we solve for the dimensionless occupation density $p(r,\theta,t)$ by transforming to Laplace space $\hat{p}(r,\theta,s) = \int_{t=0}^{\infty} p(r,\theta,t)\, e^{-st}dt$, to see that (A.52b) satisfies the PDE

$$(A.53) \qquad \hat{p}_{rr} + \frac{1}{r}\hat{p}_r + \frac{1}{r^2}\hat{p}_{\theta\theta} - s\hat{p} = -\frac{1}{r}\delta(r-R)\delta(\theta), \qquad r > 1, \quad \theta \in (-\pi,\pi), \quad s \in \mathbb{C}.$$

The separable solution that is continuous, bounded and satisfies $\hat{p}(1,\theta,s) = 0$ is

$$(A.54) \qquad \hat{p}(r,\theta,s) = \begin{cases} \displaystyle\sum_{n=0}^{\infty} A_n\left[I_n(\sqrt{s}r) - \frac{I_n(\sqrt{s})}{K_n(\sqrt{s})}K_n(\sqrt{s}r)\right]\cos n\theta, & 1 < r \le R; \\ \displaystyle\sum_{n=0}^{\infty} A_n\left[\frac{I_n(\sqrt{s}R)}{K_n(\sqrt{s}R)} - \frac{I_n(\sqrt{s})}{K_n(\sqrt{s})}\right]K_n(\sqrt{s}r)\cos n\theta, & r > R, \end{cases}$$

with constants A_n determined from incorporation of the Dirac source to be

$$(A.55) \qquad A_n = K_n(\sqrt{s}R)\left[\int_{\theta=0}^{2\pi}\cos^2(n\theta)\, d\theta\right]^{-1} = \begin{cases} \frac{1}{2\pi}K_0(\sqrt{s}R) & n = 0 \\ \frac{1}{\pi}K_n(\sqrt{s}R) & n \ge 1 \end{cases}$$

Correspondingly, the flux over $r = 1$ is given in series form by

$$(A.56) \qquad \hat{p}_r|_{r=1} = \frac{1}{2\pi}\frac{K_0(R\sqrt{s})}{K_0(\sqrt{s})} + \frac{1}{\pi}\sum_{n=1}^{\infty}\frac{K_n(R\sqrt{s})}{K_n(\sqrt{s})}\cos n\theta.$$

To invert the Laplace transform of $\hat{p}_r|_{r=1}$, we must evaluate the Bromwich integrals

$$\frac{1}{2\pi i}\int_{c-i\infty}^{c+i\infty}\frac{K_n(\sqrt{s}R)}{K_n(\sqrt{s})}e^{st}\, ds, \qquad n = 0,1,2,\dots$$

where c is chosen to lie to the right of any poles of the integrand. Since the only singularity is a branch cut on the negative real axis, we deform the contour to a hairpin along the negative real axis and introduce the substitution $s = -w^2$. The integral becomes

$$\frac{1}{\pi i}\int_0^\infty \left[\frac{K_n(i\omega R)}{K_n(i\omega)} - \frac{K_n(-i\omega R)}{K_n(-i\omega)}\right]\omega e^{-\omega^2 t}\, d\omega = \frac{2}{\pi}\int_0^\infty \left[\frac{J_n(\omega)Y_n(\omega R) - J_n(\omega R)Y_n(\omega)}{Y_n^2(\omega) + J_n^2(\omega)}\right]\omega e^{-\omega^2 t}\, d\omega,$$

where we have used $K_n(-iz) = \frac{\pi}{2}[-Y_n(z) + iJ_n(z)]$. The expression for the flux $\mathcal{J}(t,\theta) = p_r|_{r=1}$ is now

$$(A.57a) \qquad \mathcal{J}(t,\theta) = \frac{1}{2\pi}\chi_0(t) + \frac{1}{\pi}\sum_{n=1}^\infty \chi_n(t)\cos n\theta, \qquad \theta \in (-\pi,\pi), \quad t > 0,$$

where the coefficients are

$$(A.57b) \qquad \chi_n(t) = \frac{2}{\pi}\int_0^\infty \left[\frac{J_n(\omega)Y_n(\omega\mu) - J_n(\omega\mu)Y_n(\omega)}{Y_n^2(\omega) + J_n^2(\omega)}\right]\omega e^{-\omega^2 t}\, d\omega.$$

The total flux to the inner disk, and distribution of arrival times, is given by

$$(A.58) \qquad \chi_0(t) = \int_0^{2\pi} \mathcal{J}(t,\theta)\, d\theta = \frac{2}{\pi}\int_0^\infty \left[\frac{J_0(\omega)Y_0(\omega R) - J_0(\omega R)Y_0(\omega)}{Y_0^2(\omega) + J_0^2(\omega)}\right]\omega e^{-\omega^2 t}\, d\omega.$$

Returning to dimensional time through (A.52a), we have that $S(t) = \frac{D}{a^2}\chi_0(\frac{D}{a^2}t)$. To determine $C(t)$ and $P(t) = 1 - C(t)$, we note from $P'(t) = -S(t)$ that

$$(A.59) \qquad P(t) = 1 - \int_0^{\frac{D}{a^2}t} \chi_0(\eta)\, d\eta, \qquad C(t) = \int_0^{\frac{D}{a^2}t} \chi_0(\eta)\, d\eta.$$

For the dimensional arrival time $t = t^*$, the conditional distribution of arrival angles θ is then given by $\mathcal{J}(\frac{D}{a^2}t^*,\theta)/\chi_0(\frac{D}{a^2}t^*)$ with cumulative distribution

$$(A.60) \qquad F(\theta;t_*) = \int_{-\pi}^\theta \frac{\mathcal{J}(\frac{D}{a^2}t_*,\eta)}{\chi_0(\frac{D}{a^2}t_*)}\, d\eta = \frac{\theta + \pi}{2\pi} + \frac{1}{\pi}\sum_{n=1}^\infty \frac{\chi_n(\frac{D}{a^2}t_*)}{n\chi_0(\frac{D}{a^2}t_*)}\sin n\theta, \qquad \theta \in (-\pi,\pi).$$

References.

[1] Joseph Abate and Ward Whitt, *A Unified Framework for Numerically Inverting Laplace Transforms*, INFORMS J. on Computing, 18 (2006), pp. 408–421.

[2] C. G. Adams, J. H. Schenker, P. S. McGhee, L. J. Gut, J. F. Brunner, and J. R. Miller, *Maximizing Information Yield From Pheromone-Baited Monitoring Traps: Estimating Plume Reach, Trapping Radius, and Absolute Density of Cydia pomonella (Lepidoptera: Tortricidae) in Michigan Apple*, Journal of Economic Entomology, 110 (2017), pp. 305–318.

[3] Lazaros Batsilas, Alexander M Berezhkovskii, and Stanislav Y Shvartsman, *Stochastic model of autocrine and paracrine signals in cell culture assays*, Biophysical Journal, 85 (2003), pp. 3659–3665.

[4] Alexander M Berezhkovskii, Leonardo Dagdug, Vladimir A Lizunov, Joshua Zimmerberg, and Sergey M Bezrukov, *Trapping by clusters of channels, receptors, and transporters: Quantitative description*, Biophysical Journal, 106 (2014), pp. 500–509.

[5] H. C. Berg, *Random Walks in Biology*, Princeton University Press, 1993.

[6] P.C. Bressloff, *Asymptotic analysis of target fluxes in the three-dimensional narrow capture problem*, Multiscale Model. Simul., 19 (2021), pp. 612–632.

[7] P. C. Bressloff, *Asymptotic analysis of extended two-dimensional narrow capture problems*, Proceedings of the Royal Society A: Mathematical, Physical and Engineering Sciences, 477 (2021), p. 20200771.

[8] Paul C. Bressloff and Jay M. Newby, *Stochastic models of intracellular transport*, Rev. Mod. Phys., 85 (2013), pp. 135–196.

[9] Roman Chapko and Rainer Kress, *Rothe's Method for the Heat Equation and Boundary Integral Equations*, Journal of Integral Equations and Applications, 9 (1997), pp. 47–69.

[10] S. Jonathan Chapman, David P. Hewett, and Lloyd N. Trefethen, *Mathematics of the faraday cage*, SIAM Review, 57 (2015), pp. 398–417.

[11] A. Cheviakov and M. J. Ward, *Optimizing the Principal Eigenvalue of the Laplacian in a Sphere with Interior Traps*, Math. and Comp. Model., 53 (2011), pp. 1394–1409.

[12] S.H. Chiu, M.N.J. Moore, and B. Quaife, *Viscous transport in eroding porous media*, Journal of Fluid Mechanics, 893 (2020).

[13] Mark de Berg, Otfried Cheong, Marc van Kreveld, and Mark Overmars, *Computational Geometry, Algorithms and Applications*, Springer, 2008.

[14] W. Dijkstra and M.E. Hochstenbach, *Numerical approximation of the logarithmic capacity*, CASA-report, Technische Universiteit Eindhoven, 2008.

[15] U. Dobramysl and D. Holcman, *Mixed analytical-stochastic simulation method for the recovery of a brownian gradient source from probability fluxes to small windows*, Journal of Computational Physics, 355 (2018), pp. 22 – 36.

[16] L. Greengard and J.-R. Li, *High Order Accurate Methods for the Evaluation of Layer Heat Potentials*, SIAM Journal on Scientific Computing, 31 (2009), pp. 3847–3860.

[17] D. Holcman and Z. Schuss, *The Narrow Escape Problem*, SIAM Review, 56 (2014), pp. 213–257.

[18] Chi-Ok Hwang and Michael Mascagni, *Electrical capacitance of the unit cube*, Journal of Applied Physics, 95 (2004), pp. 3798–3802.

[19] Samuel A. Isaacson and Jay Newby, *Uniform asymptotic approximation of diffusion to a small target*, Phys. Rev. E, 88 (2013), p. 012820.

[20] S. Iyaniwura and M. J. Ward, *Asymptotic Analysis for the Mean First Passage Time in Finite or Spatially Periodic 2-D Domains with a Cluster of Small Traps*, preprint, (2021).

[21] S. Iyaniwura, T Wong, M. J. Ward, and Maconald C., *Optimization of the Mean First Passage Time in Near-Disk and Elliptical Domains in 2-D with Small Absorbing Traps*, SIAM Review, 63 (2021), pp. 525–555.

[22] ——, *Simulation and Optimization of Mean First Passage Time problems in 2D using Numerical Embedded Methods and Perturbation Theory*, SIAM J. Multiscale Modeling and Simulation, 19 (2021), pp. 1367–1393.

[23] M.C. Kropinski and B.D. Quaife, *Fast integral equation methods for Rothe's method applied to the isotropic heat equation*, Computers and Mathematics with Applications, 61 (2010), pp. 2436–2446.

[24] Venu Kurella, Justin C. Tzou, Daniel Coombs, and Michael J. Ward, *Asymptotic Analysis of First Passage Time Problems Inspired by Ecology*, Bulletin of Mathematical Biology, 77 (2015),

pp. 83–125.

[25] Sean D. Lawley, Alan E. Lindsay, and Christopher E. Miles, *Receptor Organization Determines the Limits of Single-Cell Source Location Detection*, Phys. Rev. Lett., 125 (2020), p. 018102.

[26] Sean D. Lawley and Jacob B. Madrid, *A probabilistic approach to extreme statistics of brownian escape times in dimensions 1, 2, and 3*, Journal of Nonlinear Science, 30 (2020), pp. 1207–1227.

[27] A. E. Lindsay, A. J. Bernoff, and D.D Schmidt, *Boundary homogenization and capture time distributions of semi-permeable membranes with periodic patterns of reactive sites*, Submitted, Multiscale Modeling and Simulation, (2018).

[28] A. E. Lindsay, A. J. Bernoff, and M. J. Ward, *First Passage Statistics for the Capture of a Brownian Particle by a Structured Spherical Target with Multiple Surface Traps*, Multiscale Modeling and Simulation, 15 (2017), pp. 74–109.

[29] A. E. Lindsay, T. Kolokolnikov, and J. C. Tzou, *Narrow escape problem with a mixed trap and the effect of orientation*, Phys. Rev. E, 91 (2015), p. 032111.

[30] A. E. Lindsay, R.T. Spoonmore, and J.C. Tzou, *Hybrid asymptotic-numerical approach for estimating first passage time densities of the two-dimensional narrow capture problem*, Phys. Rev. E, 94 (2016), p. 042418.

[31] S Litwin, *Monte Carlo simulation of particle adsorption rates at high cell concentration.*, Biophysical Journal, 31 (1980), p. 271.

[32] J.R. Miller, C.G. Adams, P.A. Weston, and J.H. Schenker, *Trapping of Small Organisms Moving Randomly*, Springer, 2015.

[33] Scott H. Northrup, *Diffusion-controlled ligand binding to multiple competing cell-bound receptors*, The Journal of Physical Chemistry, 92 (1988), pp. 5847–5850.

[34] Tomas Opplestrup, Vasily V. Bulatov, George H. Gilmer, Malvin H. Kalos, and Babak Sadigh, *First-passage Monte Carlo algorithm: Diffusion without all the hops*, Physical Review Letters, 97 (2006).

[35] F. Paquin-Lefebvre, S. Iyaniwura, and M.J Ward, *Asymptotics of the principal eigenvalue of the laplacian in 2d periodic domains with small traps*, European Journal of Applied Mathematics, (2021), pp. 1–28.

[36] S. Pillay, M. J. Ward, A. Peirce, and T. Kolokolnikov, *An Asymptotic Analysis of the Mean First Passage Time for Narrow Escape Problems: Part I: Two-Dimensional Domains*, SIAM Multiscale Modeling and Simulation, 8 (2010), pp. 803–835.

[37] Bryan Quaife and M. Nicholas J. Moore, *A boundary-integral framework to simulate viscous erosion of a porous medium*, Journal of Computational Physics, 375 (2018), pp. 1–21.

[38] Metzler R., Oshanin G., and S. Redner, eds., *First-Passage Phenomena and Their Applications*, World Scientific, 2014.

[39] S. Redner, *A Guide to First-Passage Processes*, Cambridge University Press, 2001.

[40] Salma Saddawi and William Strieder, *Size effects in reactive circular site interactions*, The Journal of Chemical Physics, 136 (2012), p. 044518.

[41] T.P. Schulze, *Kinetic monte carlo simulations with minimal searching*, Physical Review E, 65 (2002).

[42] ——, *Efficient kinetic monte carlo simulation*, Journal of Computational Physics, 227 (2008), pp. 2455–2462.

[43] Avram Sidi and Moshe Israeli, *Quadrature Methods for Periodic Singular and Weakly Singular Fredholm Integral Equations*, Journal of Scientific Computing, 3 (1988), pp. 201–231.

[44] Tracy L. Stepien, Cole Zmurchok, James B. Hengenius, Rocío Marilyn Caja Rivera, Maria R. D'Orsogna, and Alan E. Lindsay, *Moth mating: Modeling female pheromone calling and male navigational strategies to optimize reproductive success*, Appl. Sci., 10 (2020).

[45] William Strieder, *Interaction between two nearby diffusion-controlled reactive sites in a plane*, The Journal of Chemical Physics, 129 (2008), p. 134508.

[46] Y. Sun, R. Caflisch, and B. Engquist, *A multiscale method for epitaxial growth*, SIAM Multiscale Model. Simul., 9 (2011), pp. 335–354.

[47] Lloyd N. Trefethen, *Series Solution of Laplace Problems*, The ANZIAM Journal, 60 (2018), p. 1–26.

[48] L. N. Trefethen, J. A. C. Weideman, and T. Schmelzer, *Talbot quadratures and rational approximations*, BIT Numerical Mathematics, 46 (2006), pp. 653–670.

[49] J. A. C. Weideman, *Optimizing Talbot Contours for the Inversion of the Laplace Transform*, SIAM Journal on Numerical Analysis, 44 (2006), pp. 2342–2362.

[50] Jui-Chuang Wu and Shih-Yuan Lu, *Patch-distribution effect on diffusion-limited process in dilute suspension of partially active spheres*, The Journal of Chemical Physics, 124 (2006), p. 024911.